Materials Advances

ROYAL SOCIETY OF CHEMISTRY

REVIEW

View Article Online
View Journal | View Issue

Cite this: *Mater. Adv.*, 2022, 3, 8030

Morphological evolution driven semiconducting nanostructures for emerging solar, biological and nanogenerator applications

Avanish Kumar Srivastava,[ab] Jai Shankar Tawale,[c] Rajni Verma,[d] Daksh Agarwal,[ef] Charu Sharma,[ab] Ashavani Kumar[g] and Manoj Kumar Gupta *[ab]

Metal oxide nanostructures are extremely fascinating smart and functional materials owing to their outstanding wide and tunable band gap, biocompatibility, high electrochemical coupling coefficient, high photostability, high sensitivity, non-toxicity, high electron mobility and high thermal/chemical stability properties. The morphologies of the metal oxide nanostructures are highly influenced by growth parameters and methods. The performance of solar cell/sensors, biological, electronic and energy harvesting properties are highly varied with the morphological changes in the nanostructures. The progress of the metal oxide nanostructures for particular applications has been discussed in many earlier review articles; however, a comprehensive review article based on the various morphologies of metal oxide nanostructures (especially, together with ZnO and SnO_2) for their numerous and next-generation applications has not been reported yet. The present review article summarizes the recent progresses and applications of ZnO and SnO_2 nanostructures to provide a comprehensive understanding of the effect of morphologies on the performance of the technological devices and biosensors. The growth of various nanostructures (such as tetrapods, nanorods and nanowires) and their wide applications in solar cells, biological field, sensors and piezoelectric nanogenerators/piezotronics are covered in the present review. This review also provides a detailed comparison of the performances of ZnO nanostructure-based solar cells with SnO_2-based solar cells and flexible devices. The performance of the solar cell in terms of morphology, electron mobility, band gap and piezoelectric properties are also discussed. This paper also gives insights into the antimicrobial, antilarvicidal and anticancer activities of various ZnO and SnO_2 nanostructures. In addition, special deliberation has been made on the fabrication of novel piezoelectric nanogenerators based on the various morphologies of ZnO (such as nanowires, nanosheets and nanorods) for scavenging mechanical energy from the living environment. Finally, the benefits, challenges and future outlook of metal oxide nanostructures for their potential application in opto-electronic, sensors, biomedical energy harvesting and next-generation flexible self-powered nanosystems are highlighted.

Received 14th June 2022,
Accepted 14th September 2022

DOI: 10.1039/d2ma00683a

rsc.li/materials-advances

1. Introduction

Presently, the emerging field of nanoscience, nanoengineering, nanoelectronics and nanomaterials has played a significant commercial and social impact towards solutions for energy, sensor, health and environmental concerns.[1,2] In recent years, metal oxide nanomaterials have received much attention because of their outstanding structural, electrical and optical properties, which made them attractive materials for numerous potential applications in several sectors, such as optics, energy, electronics, dielectric, biomedical and photonics.[2] Metal oxide nanostructures in a wide number of morphologies (such as nanobelts, nanoflowers, nanotubes, nanorings, and nanowires) have been synthesized and reported by various authors worldwide.[2,3]

[a] *CSIR-Advanced Materials and Processes Research Institute, Bhopal, Madhya Pradesh 462026, India. E-mail: mkgupta@ampri.res.in; Fax: +91 755-2457042; Tel: +91 9977360351*
[b] *Academy of Scientific and Innovative Research (AcSIR), Ghaziabad-201002, India*
[c] *CSIR-National Physical Laboratory, New Delhi-110012, India*
[d] *School of Physics, The University of Melbourne, Parkville, Victoria 3010, Australia*
[e] *Department of Materials Science and Engineering, University of Pennsylvania, Philadelphia, PA 19104, USA*
[f] *Lam Research Corporation, Fremont, CA 94538, USA*
[g] *Department of Physics, National Institute of Technology Kurukshetra, Haryana, 136119, India*

To understand the fundamental phenomena in low-dimensional systems and to develop the next-generation nanodevices for solar, sensor, energy and biomedical applications with high performance, the synthesis of metal oxide nanostructures is highly beneficial. The nanomaterials are distinguished on the basis of their size and they are synthesized by various novel synthesis approaches, where a reduced dimension at the nanoscale can alter or enhance their physical, chemical and electronic properties, which are the basis of science and nanotechnology.[1–5] The nanomaterials are broadly classified on the basis of dimensionality, origin and needs of the 21st century for a variety of societal applications. The uniform size distribution in nano-structural materials along with size and morphology play an important role in controlling the optical and sensing properties, which have decisive roles in future nanotechnology, for manufacturing smart and efficient devices.[6–14] A structure that has confinement in all three dimensions (x, y, z) at the nanoscale is called a 0 (zero)-D structure. The nanoparticles or quantum dots (including single crystalline, polycrystal nature and amorphous) with various morphologies of discs, sheets, cubes and platelets reveal quantum confinement in all three dimension to some extent.[15] Nanomaterials with single crystallinity are often known as nanocrystals. If all three dimensions of the nanocrystals are confined to the 1–10 nm scale, the crystal is termed as a quantum dot.[16–25] Whiskers and fiber-like structures with diameters ranging from a few nanometers to several hundred nanometers are known as one-dimensional nanostructures. Thus, nanowires and nanorods are referred to as one-dimensional (1-D) nanostructures with diameter in the nanoscale range and length in few hundred nanometers. Morphologies, such as the nano-belt, tube, comb,

Avanish Kumar Srivastava

Dr Avanish Kumar Srivastava received his Master's degree from IIT Roorkee, MTech from IIT Kanpur, and doctorate from IISc, Bangalore, India in metallurgy science. He is presently working as the Director at CSIR-Advanced Materials and Processes Research Institute (CSIR-AMPRI) Bhopal, Madhya Pradesh, India and Director (Additional Charge) CSIR-National Metallurgical Laboratory Jamshedpur Jharkhand, India. He has expertise in the growth of semiconducting, metal oxide and perovskite nanomaterials materials, and their characterization and evaluation of various properties through electron microscopes. He is President of the Electron Microscope Society of India. He has authored more than 350 international articles. He recieved various awards including NMD-2011 and NRDC-2020.

Jai Shankar Tawale

Dr Jai Shankar Tawale received his PhD degree in Physics from the National Institute of Technology (NIT) Kurukshetra, Haryana. He is currently working in the Indian Reference Materials Division (BND) at CSIR-National Physical Laboratory, New Delhi. His current research interest includes oxide nanomaterials and their composites, reference materials, and characterization of nanomaterials, and has published more than 35 research articles.

Rajni Verma

Dr Rajni Verma received her PhD in 2018 from the CSIR-National Physical Laboratory, India, for her research on the synthesis and applications of various nanomaterials. As a postdoctoral researcher, she worked at the Indian Institute of Technology Delhi in metal organic frameworks for photocatalytic applications. After that, she was awarded a prestigious McKenzie Fellowship in 2019, and her research interest is currently focused on the nano-bio interface at the School of Physics, The University of Melbourne, Australia.

Daksh Agarwal

Dr Daksh Agarwal is presently working at the Technology Development group at Lam Research, USA. He obtained a PhD degree from the University of Pennsylvania in Material Science and Engineering in 2016. His current research interest includes oxide nanomaterials, and their application in energy and sensors. He has more than 20 research articles in reputed journals.

needle and cables, are considered 1-D nanostructures. The nanorods are about 10 000 times smaller than the human hair and are packed together in such a way that light particles cannot pass through them, resulting in most of the light being absorbed.[26–30] In addition, in 2D materials, one of the dimensions is nanoscale (confined in one direction only) and the other dimension varies in the micrometer scale. Thin film or layer structures deposited on various substrates of any composition and being crystalline/amorphous in nature are considered 2-D nanomaterials. Two-dimensional (2-D) nanostructures include plates, sheets, triangles, single and multilayer films and transparent coating type. Accordingly, graphene as one-atom thick plane sheet of carbon is the best example of a two-dimensional nanostructure. The 2D materials demonstrated various unique properties, such as excellent superconductivity, new electronic and physical properties, along with florescence properties. The anisotropic transport properties of the 2D materials hold promising applications in devices covering solar cells, UV sensors, touch screens, electronic gadgets and smart mobile phones. The 2-D nanostructures alone or combined with other materials as a composite have potential to play a leading role in incredible future technologies.[31,32] In addition to that, polycrystals or bulk materials with three arbitrary dimensions of more than 100 nm size of nanosized crystals are three-dimensional (3-D) nanostructures. Among the various nanostructures, metal oxide nanostructures (including, ZnO and SnO/SnO_2) have recently attracted huge interest due to their proven technological, medical and industrial applications.[30–32] Fig. 1 shows the schematic image of the application of the metal oxide nanostructures in numerous sectors, including automobile, optical, biological, sensors, solar and piezoelectric nanogenerators. In the present review, we specially cover the synthesis of various morphologies of the ZnO and SnO_2-based nanostructure, and their sensing, solar, energy and biomedical applications are discussed. Moreover, the article provides a comprehensive review on the recent development in the synthesis, optical, humidity sensing and energy applications of ZnO and SnO_2 nanostructures and their composites with polymers. A brief survey on the cost-effective and mixed synthesis approach to obtain several crystalline nanostructures with tunable morphological and properties is also included. Several metal oxide morphologies of ZnO and SnO_2, such as nanorods, tetrapods, spherical, flower, octahedral shape geometry and their mixed counterpart with graphene layers for specific applications in future nanotechnology have been discussed. The effects of impurities, doping and

Charu Sharma

Ms Charu Sharma received her Bachelor in Science (BSc) degree from Regional Institute of Education, Ajmer (India) and Masters degree in Applied Physics from Babasaheb Bhimrao Ambedkar University, Lucknow (India). She is a Gold Medalist. Currently, she is pursuing a PhD under the supervision of Dr Manoj Kumar Gupta and Dr Avanish Kumar Srivastava from the Academy of Scientific and Innovative Research-Advanced Materials and Processes Research Institute (AcSIR-AMPRI), Bhopal (India). Her research interest is mainly focused on the synthesis of two-dimensional nanomaterials and its application as a piezoelectric energy harvester.

Ashavani Kumar

Dr Ashavani Kumar is Professor & Head, Department of Physics, National Institute of Technology Kurukshetra, India. He received a PhD degree in Physics (1994) from Aligarh Muslim University, Aligarh, India. He has been in academics, research and administration for over 30 years. His research activities cover high-energy physics, instrumentation, materials engineering and nanotechnology for various applications. He has published more than 100 research papers in international reputed journals and contributed more than 200 papers in proceedings. Dr Kumar was awarded the International Postdoctoral Fellowship in Experimental Physics (OPEN) by the National Institute for Nuclear Physics (INFN-Fellowships), Govt. of Italy. Dr Kumar also has other administrative responsibilities in the institute.

Manoj Kumar Gupta

Dr Manoj Kumar Gupta received his PhD degree from the University of Delhi, India, in 2011. Presently, he is working as a Scientist at CSIR-Advanced Materials and Processes Research Institute (CSIR-AMPRI) Bhopal. He was awarded the CSIR-Young Scientist Award in Physical Science (Including Instrumentation) and CSIR Raman Research Fellowship. He also holds a DST-INSPIRE Faculty fellowship. He worked as a postdoctoral fellow at Sungkyunkwan University, South Korea from 2014 to 2017. He has visited various countries and given various scientific talks in USA, China and Finland. His current research areas are nano-materials synthesis and fabrication of energy harvesting nanodevices, such as piezoelectric, pyroelectric, triboelectric and hybrid nanogenerators and polymer composites. He has more than 60 international publications in reputed journals and has five international patents.

Fig. 1 Various potential and industrial applications of metal oxide nanostructures.

composite nanostructures are also reviewed for new morphological designs based on metal oxide nanostructures to explore new directions in the field of advanced research in the forthcoming technologies. The fabrication of the flexible piezoelectric nanogenerator based on the ZnO and SnO_2 nanostructures to convert mechanical vibrations from living environments is also discussed.

2. Synthesis of metal oxide nanostructures (ZnO and SnO_2)

The preparation of nanostructure materials is one of the most important, challenging and crucial tasks for designing novel devices for specific applications. The synthesis of metal oxide nanomaterials with desired morphology and composition have stimulated great interest to fabricate efficient nano-devices for different applications. The morphological design includes various intriguing nanostructures, like particles, tubes, rods, needles, plate, sheet, ribbon, tetrapod, flower, octahedral and many other shapes. Controlling the growth formation and reproducibility of these nanostructures in terms of the uniform size distribution, identical in shape and elemental composition is an equally important and challenging task. Several growth techniques/methods have been reported to fabricate metal oxide nanostructure morphologies using top-down and bottom-up methods. In the bottom-up approach, molecular components arrange themselves into a more complex assembly atom-by-atom, molecule-by-molecule, and cluster-by-cluster from the bottom. Synthesis of nanoparticles by colloid dispersions is an example of the bottom-up approach. This approach is crucial and important to fabricating various dimensional nanostructures of small size and shape. The bottom-up approach offers a molecular-level and fabrication strategy that can be controlled for synthesis and nanoelectronic devices, which are not usually possible with top-down methods.[33] In the top-down approach, nanosized structures or particles are prepared by breaking down the bulk material into nanoscale materials though various techniques.[34] Moreover, recent hybrid nano manufacturing strategies that combine the advantages of both top-down and bottom-up approaches are being used for the large-scale and cost-effective generation of metal oxide nanostructures.[35]

Various physical and chemical routes (such as thermal evaporation, laser ablation, hydrothermal route, template base synthesis, and sol–gel) have recently been employed to synthesize metal oxide nanostructures with the desired morphology for different properties and applications.[36] This includes the example of the bottom up synthesis method, wherein the chemical routes are chosen to generate different nanostructures on a large scale and by controlling the growth parameters. The physical routes are more challenging, but a popular route to fabricate nanostructures at the large scale of the required structural morphology. Physical vapor deposition (PVD), which includes the condensation and evaporation of a material on a substrate in the form of a coating having a thickness in the nano-micro range, is an example of the top up approach. This method is also popular due to the high crystallinity and uniform quality of the nanomaterials. The thermal evaporation method is also used to achieve the metal oxide nanostructures due to its simple and economical properties. The thermal evaporation process involves

sublimation of the source material at high temperature, and subsequent deposition of the vapor on certain substrates in a specific temperature region is used to achieve the required nanostructures. Recently, the flower-like ZnO nanorod was successfully developed by thermal evaporation without the use of any catalyst or template.[37] The nano- and micron sizes of the ZnO with nanorod- and nanoparticle-like morphologies have been produced by the thermal evaporation method.[38–40] The ZnO nanowires array was synthesized by thermal evaporation directly on a Zn foil.[41] The ZnO tetrapods are also grown by the sublimation process by employing thermal evaporation to achieve optical properties and antibacterial applications.[42–44] Moreover, the urchin-like morphology of the ZnO nanorods has also been reported by solution technique.[43,44] Nanostructures with fascinating morphologies like the tetrapods and nanowires of ZnO have been successfully produced by the CVD method.[44] Similarly, a cost-effective and simple thermal evaporation process was successfully employed to produce various morphologies of SnO_2 nanostructures for optoelectronic, sensing and energy applications.[45–54] The CVD-grown SnO_2 nanostructures for optical and sensor applications have been also reported.[45] The sol–gel approach is a well-known and popular process for the successful synthesis of various metal oxide nanomaterials.[55] The sol–gel technique was widely used to fabricate dimensionally confined nanostructures of ZnO.[56,57] The rich families of ZnO and SnO_2 morphologies (including nanowires, nanotubes, nanorods and nanocrystals) were prepared by sol–gel method for various applications.[58–63] The sol–gel method was also employed to produce bare and doped SnO_2 nanostructures for many applications with enhanced performance.[64–71] Moreover, the hydrothermal approach is widely used by researchers to obtain metal oxide nanostructures. These hydrothermally synthesized nanomaterials have been largely incorporated in composite nanomaterials to enhance the nanoscale materials properties. The ZnO and SnO_2 nanostructures were successfully prepared by hydrothermal method for various morphologies and many nanoscale device properties. ZnO-reinforced polyaniline nanocomposite nanomaterials prepared by microwave-assisted hydrothermal synthesis for electrically conductive properties have also been reported.[72] SnO_2 backbone and ZnO nanostructures with hierarchical assembly by low-temperature hydrothermal synthesis approach have also been reported for optical applications.[73–77]

In addition, the combustion synthesis technique is a powerful route for the synthesis of nanostructures.[77] The combustion method is a low-temperature, time-saving, energy efficient, self-propagating method, and involves a spontaneous exothermic redox reaction between a metal nitrate and organic fuel that is used to prepare nanomaterials. The method is based on the utilization of the heat energy produced during the exothermic spontaneous redox reaction between an oxidizer and reducing agent. The combustion method is emerging as a facile and economically viable technique, and was successfully used in the preparation of a large number of technologically useful oxides and nanomaterials.[78–88] In addition to these novel synthesis methods, mixed strategies including physical and chemical routes are used to fabricate different nanomaterials. Currently, the hybrid synthesis is a popular approach to achieve the desired nanostructures through both chemical and physical efforts. The process is useful for the synthesis of composite nanostructures consisting of organic–inorganic hybrids. The incorporation of organic compounds into an inorganic matrix through either physical trapping or chemical bonding modifies various physical properties. However, the challenge is to prevent phase segregation of the nanomaterials. The intercalation process is recommended for the incorporation of guest species (atom, molecules and ions) in a layered crystalline host matrix, preserving the structural integrity of the host lattice.

2.1. ZnO nanostructure

In the last few decades, there has been growing importance of nanotechnology for high-end technological solutions. Furthermore, the study on the dimensional confinement of ZnO nanomaterials became a growing area in the nanotechnological advancement. ZnO is a popular piezoelectric, non-toxic and semiconducting metal oxide material with high electron mobility, large band gap and high diffusion coefficient. ZnO can be easily synthesized in several morphologies,including nanotubes, nanoflowers, nanorods, nanowires, nanocrystals and nanospheres.[78] The ZnO nanostructure has been utilized for various ranges of applications, such as sensors, catalyst, solar cells, supercapacitors, surface coatings, biological, batteries, photodetectors and piezoelectric nanogenerators.

ZnO exhibits wurtzite and zinc blende crystal structures. The wurtzite structure of ZnO is the most thermodynamically stable phase. ZnO has a hexagonal unit cell with the following lattice parameters: a = 0.324 and c = 0.520 nm (wurtzite). The ZnO structure can be understood as a cation (Zn^{2+}) surrounded by four (O^{2-}) anions at the corners of a tetrahedron (Fig. 2).[89] ZnO is a key technological material, and the synthesis of the ZnO nanostructures has become a hot area of research due to its proven potential applications as UV sensors, nanogenerators, solar cells and transducers.[90–92]

ZnO has characteristics polar surfaces with a basal plane as a common polar surface. The positively charged Zn-(0001) and negatively charged O-(000$\bar{1}$) surfaces form spontaneous polarization along the c-axis, and creates a normal dipole moment. To maintain a stable structure, the polar surfaces usually exhibit massive surface reconstructions. However, ZnO-$\pm$(0001) are atomically flat, stable, and form without reconstruction.[93,94] These unique structural properties make ZnO as a functional nanomaterial for advanced applications. The nanorods, nanowires, nanoring, nanospring, nanocomb, nanocages, nanotetrapods and many more morphologies of ZnO bring extraordinary changes in the material properties.[89,95,96]

Among various morphologies, the tetrapod shape-like nanostructure has several advantages over the other morphologies of ZnO or its bulk counterpart because of its spatial distribution between the arms. One of the key advantages of the tetrapod morphology is its automatic orientation on the substrate with one of its arms directed to the surface of the substrate. The tetrapod is the simplest structure consisting of

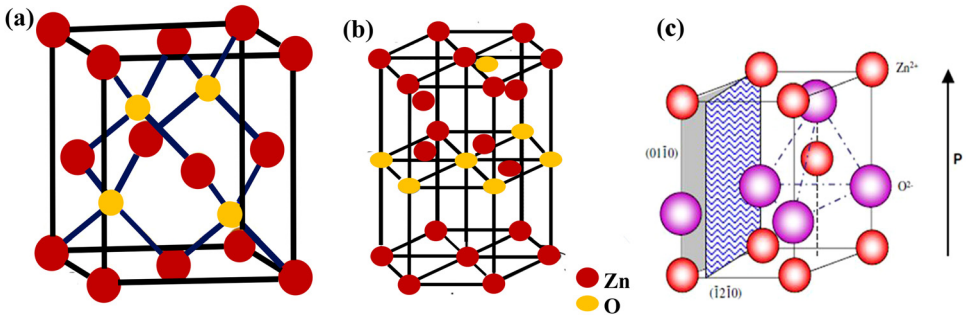

Fig. 2 (a) The zinc blende crystal structure of ZnO. (b) The wurtzite crystal structure of ZnO. (c) The wurtzite structure model of ZnO showing the tetrahedral arrangement of Zn and O in the ZnO crystal structures. Reprinted with permission from ref. 89. Copyright 2004 IOP Science.

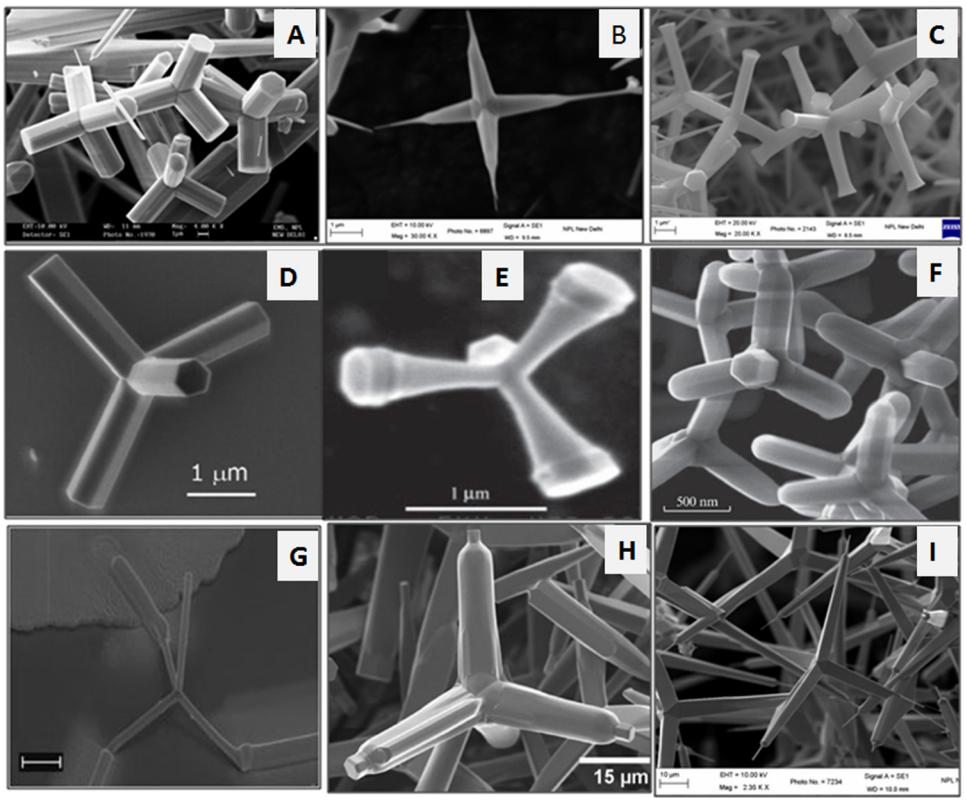

Fig. 3 Tetrapod morphologies of the ZnO nanostructures (a–c) prepared by thermal evaporation method. (d) SEM image of a single tetrapod. Reprinted with permission from ref. 96. Copyright 2007 Elsevier. (e) Trumpet-shaped ZnO tetrapod. Reprinted with permission from ref. 104. Copyright 2003 John Wiley and Sons. (f) Tetrapod morphology. Reprinted with permission from ref. 105. Copyright 2019 Springer Nature. (g) Tetrapod with electrodes for IV measurements. Reprinted with permission from ref. 106. Copyright 2006 AIP Publishing. (h) Tetrapod structure. Reprinted with permission from ref. 107. Copyright 2015 American Chemical Society. (i) Tetrapod structure with a fine tip at the end.

rod-shaped structures joined at a tetrahedral angle to the central core.[53,97–100] Various researchers have reported the growth of the ZnO tetrapod *via* various routes. The nucleation and growth kinetics of the ZnO enable it to crystallize in both hexagonal wurtzite and cubic blende structure, allowing the formation of the tetrapod-like morphology, where the four-wurtzite hexagonal arm extends to the surrounding space to form a central zinc blende core structure.[101,102] The wurtzite and zinc blende structure of ZnO forms the shared intermediate facets between the two crystal structures. This leads to the formation of the tetrapod geometry.[103] During the nucleation and growth process, the stability of these two crystal structures is important for the formation of the tetrapod structure. During the nucleation process, the zinc blende structure formation takes places. However, it is dominated by the wurtzite structure. This tetrapod structural design has the capability to form a good network with tailored mechanical strength. The tetrapod structural morphology of the ZnO nanostructures is displayed in Fig. 3.

If all of the arms of the tetrapods are uniform and less than 100 nm, then these are termed as ZnO nanocrystals (0-D).[1]

Moreover, if the length of one of the arms of the tetrapod is less than 100 nanometers, then it is known as a 1-D nanostructure. Finally, if the lengths of the arms are random in size (from nanometer to micrometer), then it is known as a 3-D nanomaterial. However, in the literature, the tetrapod geometries of the ZnO nanostructures are mostly known as 3-D nanostructures. Several synthesis processes have been developed to obtain the ZnO tetrapod structures, including the thermal evaporation process, atmosphere-controlled oxidation, microwave radiation, catalytic oxidation and self-combustion methods.[104,108–111] To obtain the ZnO tetrapod structures, the synthesis technique is composed of two categories. The first approach is started with the solid phase leading to a solid vapor transport condensation method, and the second one is the liquid reaction process. However, there are other several crucial aspects in terms of size, quantity, quality, yield and stability of the ZnO tetrapod structures, which depend on various parameters during the synthesis process, such as the temperature, heating rate, and the evaporation pressure of the Zn and O molecules during nucleation and growth kinetics. The continuous synthesis of the ZnO tetrapod at a large scale

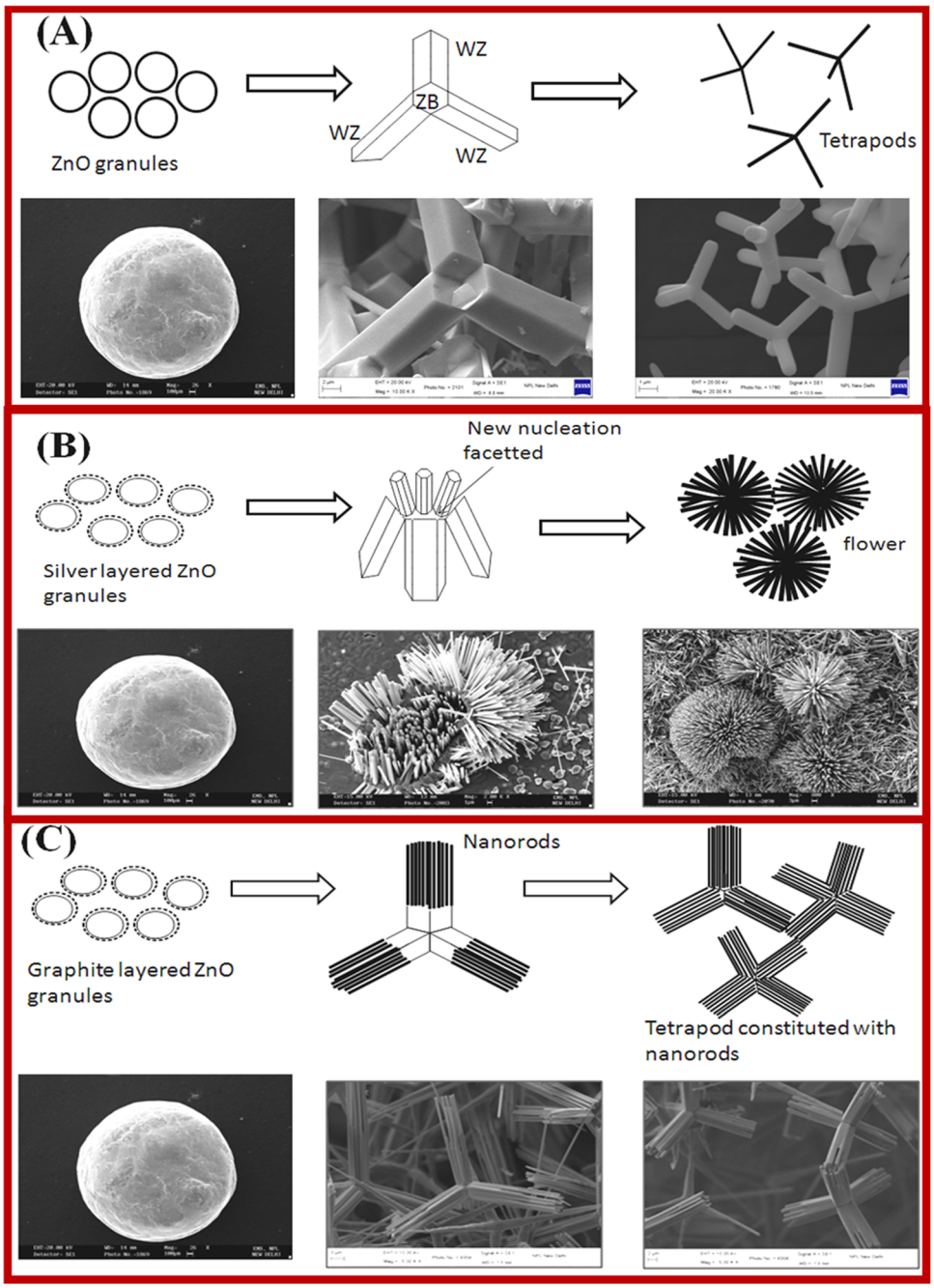

Fig. 4 Presentation of ZnO tetrapod structures nucleation and growth kinetics, and microstructural transformation with Ag and graphite doping. (a–c) ZnO, Ag-doped ZnO and Gr-doped ZnO. Reprinted with permission from ref. 116. Copyright 2013 Elsevier.

(in grams) by employing the combustion of micron-sized Zn particles was developed by S. Rackauskas *et al.* in 2015.[112] Furthermore, the ZnO tetrapod nanostructures were studied for structural modification[112,113] with optical and transport properties[114] for future nanomaterial-based devices.

J. S. Tawale *et al.* have proposed the growth mechanism of the ZnO tetrapod on the basis of the nucleation, crystal structure and surface energy.[113] The formation of the ZnO nanorod is shown in Fig. 4. Nucleation is a critical step for obtaining the required shape of the ZnO nanostructures. The crystallographic growth of the resulting structures is also governed by the formation/addition of reactive particles, which act as nucleation sites for metal reduction. This also changed the kinetics of the nanocrystal growth process. It was believed that the zinc blende phase plays a significant role in getting the tetrapod structures, which were also confirmed by HR-TEM studies.[115] It was proposed that the center of the ZnO tetrapod possesses a ZB structure, which nucleates into four arms *via* the preferred growth planes of (0002) and (1000), as shown in Fig. 4a. The strongest ionic bonding of ZnO among the group leads to the formation of the highly stable wurtzite phase, which was confirmed by XRD results. Furthermore, the growth of the flower shape morphology from the tetrapod morphology in silver (Ag)-doped ZnO is shown in Fig. 4b. The tetrapod to flower shape transformation in morphology is achieved *via* silver (Ag) doping in ZnO. As shown in Fig. 4, at the atomic level, a higher number of nucleation facets are grown. This resulted in the fast growth of other planes of the hexagonally closely packed (hcp) structure taking place, and the flower-like morphologies were formed. The doping of the Ag^{+} ions in ZnO may also be an additional nucleating agent without symmetry breaking of the hexagonal unit cell. The anisotropic growth of the flower shape ZnO structure is formed by interaction with various crystal faces.

The effect of the graphite on the structural transition in ZnO nanostructures is shown in Fig. 4c. The TEM results reveal that the tetrapod morphology of ZnO constitutes nanorods that are nucleated from the tetrapod center. The ZnO nanocrystals exhibit twin planes. The anisotropic growth and twin planes under high temperature result in the formation of a tetrahedral geometry of ZnO in the presence of highly anisotropic graphite. The controlled growth of the ZnO nanostructures with the addition of graphite and silver showed a path to overcome the challenges in the fabrication of efficient devices.[116]

As compared to other morphologies of ZnO, the multi-dimensional growth of the ZnO tetrapod makes this a fascinating material for multifunctional applications.[117] In nanoscale ZnO tetrapods, the electron conduction properties is better as compared to other morphologies for application in photovoltaic devices.[118] Various ZnO tetrapod nanostructures were also fabricated *via* different synthesis approaches, and are widely studied for sensor applications[108,119–122] and hybrid logic switches applications.[123] Moreover, the tetrapod nanocrystals have been successfully used in solar cells,[110,124,125] lasers,[126] and field emission[127] applications due to their fascinating semiconductor and absorption properties.[128] Furthermore, various efforts have been focused on tuning the electrical, optical and sensing characteristics of the ZnO tetrapod by doping. Doped ZnO tetrapods-based nano devices have also been fabricated by various researchers.[107] Similarly, ZnO tetrapod materials have successfully been used as reinforced materials for composites nanostructures. The branched nanostructure of the ZnO tetrapods is used as a reinforced material with graphene, polymers and other matrices to enhance the optical and electron transport properties for higher efficiency.

In particular, the morphology of the semiconducting piezoelectric 2D ZnO nanostructures has significantly tuned the output performance of the nanogenerators, and also altered the charge generation polarity such as from AC to DC type signals under vertical compression. 2D ZnO nanosheets have been utilized as well for 2D piezotronics device application.[129,130]

2.2 SnO_2 nanostructures and its morphological properties

Tin dioxide is an inorganic semiconductor material with the chemical formula of SnO_2. SnO_2 is also known as cassiterite and has a rutile crystal structure.[131,132] The unit cell of SnO_2 exhibits tetragonal rutile, cubic pyrite and cubic fluorite crystal structures and SnO_2 exhibits the most stable phase of the tetragonal rutile structure (Fig. 5).[132] The rutile SnO_2 has a tetragonal unit cell with a lattice constant of $a = 0.473$, $b = 0.473$ and $c = 0.318$ nm with the $P4_2/mnm$ space group. The structural geometry of the SnO_2 crystal is described as tin (Sn) atoms are six-fold and the oxygen (O) atoms are threefold coordinated. In addition, SnO_2 has high electron mobility, conductivity and high optical transparency.[131] Due to its large bandgap, high stability under heat, light and moisture conditions, and easy fabrication process, SnO_2 has been widely used in perovskite solar cells (PSCs) and dye-sensitized solar cells (DSSCs), lithium-ion batteries, supercapacitors, gas sensors and catalysis applications.

SnO_2 is an n-type semiconducting oxide nanostructure with a wide band gap of 3.6 eV at 300 K and large exciton binding energy of 130 eV. The SnO_2 possesses unique electrical and optical properties like low resistivity (10^{-4} to 10^{6}) $\Omega\ cm^{-1}$, high optical transparency and excellent chemical stability. These excellent properties make the SnO_2 nanomaterial useful for various applications, such as ceramic glazing, polishing, glass coating and in gas sensing. The bandgap of SnO_2 has been reported to be in the range of 3.5 eV to 4.0 eV. Depending on the

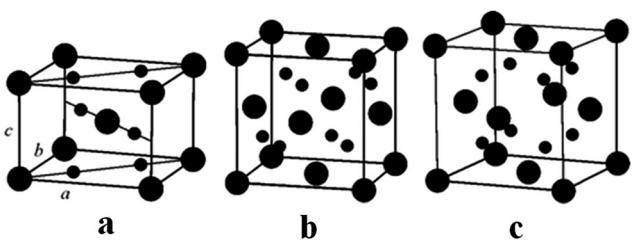

Fig. 5 Crystal structures of the SnO_2 nanostructures: (a) tetragonal rutile, (b) cubic pyrite, (c) cubic fluorite. Large and small circles represent the Sn and O atoms, respectively. Reprinted with permission from ref. 132. Copyright 2012 Springer Nature.

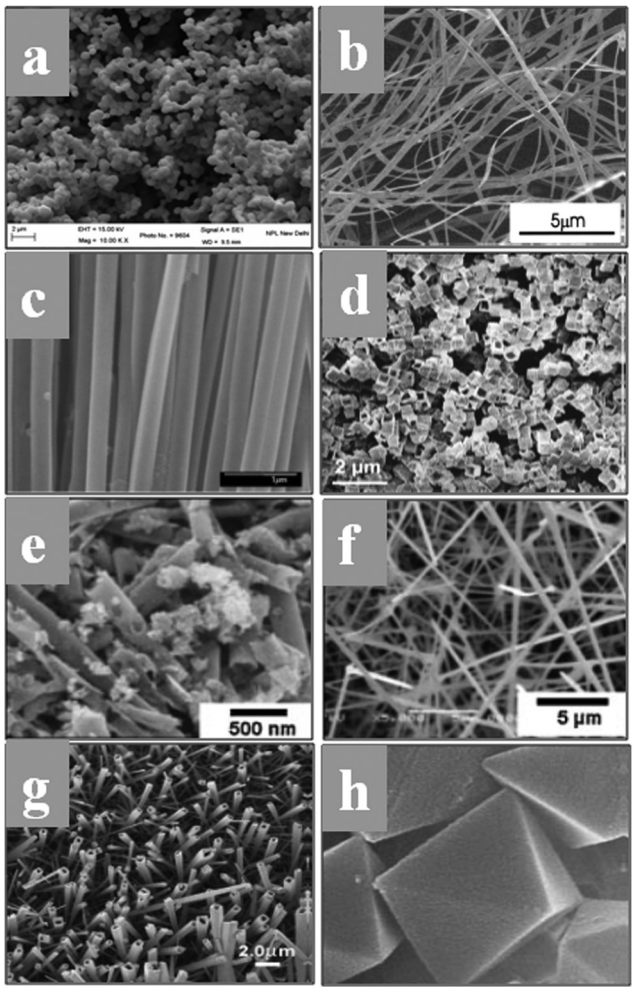

Fig. 6 (a) Faceted spherical nanostructures of SnO_2. (b) Large scale SnO_2 nanoribbons by the rapid oxidation synthesis method. Reprinted with permission from ref. 145. Copyright 2002 American Chemical Society. (c) Polycrystalline SnO_2 nanotubes prepared by infiltration casting of nanocrystallites. Reprinted with permission from ref. 146. Copyright 2005 American Chemical Society. (d) Fast formation of SnO_2 nanoboxes for energy applications. Reprinted with permission from ref. 147. Copyright 2011 American Chemical Society. (e and f) Nanotubes and nanowires of SnO_2. Reprinted with permission from ref. 148. Copyright 2008 John Wiley and Sons. (g) Array of square-shaped SnO_2 nanotubes. Reprinted with permission from ref. 149. Copyright 2005 John Wiley and Sons. (h) Self-constructed SnO_2 octahedral nanostructures based on the aggregation of nanocrystallites. Reprinted with permission from ref. 151. Copyright 2004 John Wiley and Sons.

synthesis conditions, the band gap also changes. It has a high transmittance value of 90% in glass due to the high bandgap and small refractive index. SnO_2 also has a high electron mobility of 240 $cm^2\ V^{-1}\ s^{-1}$, which is about 100 times higher than that for TiO_2. At the nanoscale, SnO_2 materials with different shapes and sizes exhibit different optical and electrical properties compared to the bulk form. The SnO_2 nanostructure has remarkable receptivity variation in gaseous environments, and it has been used for sensing and solar applications. The SnO_2 nanostructure is mostly studied for catalyst,[133] varistor,[134] field emission,[135] UV sensors,[136] sensors,[137–139] solar cells,[140,141] and lithium-ion battery applications.[142,143] The intriguing morphology of the SnO_2 nanostructures, such as nanoparticles, nanowires, nanorods, nanotubes, nanosheets, nanobox and hierarchal structures, has been successfully synthesized and reported for various applications.[144–150]

The fascinating morphology of the SnO_2 nanostructures, such as spherical, nanoribbons, nanotubes, nanobox, nanowires, square-shaped nanotubes, and octahedral (which are prepared by several novel synthesis routes), is shown in Fig. 6. The fundamental understanding about the nucleation and growth kinetics of these nanostructures (dimensional morphology) played an important role to achieve these various properties and tune their application. Furthermore, surface modifications, doping and synthesis/reaction parameters and nanostructures are major routes to change the morphology of SnO_2. There are different mechanisms discussed in the literature for the nucleation and growth kinetics of SnO_2 nanostructures. In particular, the electron microscopy technique is one of the ways to explore the growth mechanism and nucleation kinetics of nanostructures. The schematic image of the growth kinetics mechanism of the SnO_2 octahedral nanostructures is illustrated in Fig. 7.

The schematic image reveals the self-oriented growth mechanism of nanostructures on the basis of dimensional confinement (Fig. 7). The 1-D nanostructures (*e.g.*, nanorods, nanotubes) are obtained from the symmetrical accumulation of the 0-D nanostructures. Further self-orientation of these 1-D nanostructures results in 1-D or 2-D structures, depending on the interactions among the surfaces of the nanostructures during the synthesis process. In the layered structures, the stacking of layers is caused by the planar van der Waals attraction and in ionic compounds. Furthermore, these self-oriented growths of nanostructures also lead to the formation of 3-D nanostructures like spherical, tetrapod or octahedral structures. It was reported that the structural modifications in SnO_2 nanostructures have a strong influence on optical properties like absorption and defect emissions.[153–155] Various experiments have been reported, including metal ion doping in SnO_2 nanocrystals for improvement in the structural and optical properties for technological purpose.[156–158]

The sensing properties of metal oxide nanomaterials have considerable research interest because of their high surface-to-volume ratio and suitable surface chemistry for a variety of sensor applications. A sensor is basically a device that measures the physical quantity of an analyte of interest and converts it into a readable signal. For example, a humidity sensor senses, measures, and reports the relative humidity in air, and gas sensors are known for the detection of inflammable or toxic gases.[30,159,160] Owing to their low cost and flexibility in fabrication, simplicity of use, large number of detectable gases and possible application, the semiconducting oxide nanomaterials are one of the most investigated groups for sensing properties. Oxide nanostructures with modified structural, optical and electrical properties have opened up the potential application in sensor devices with high sensing, low detection limits, low

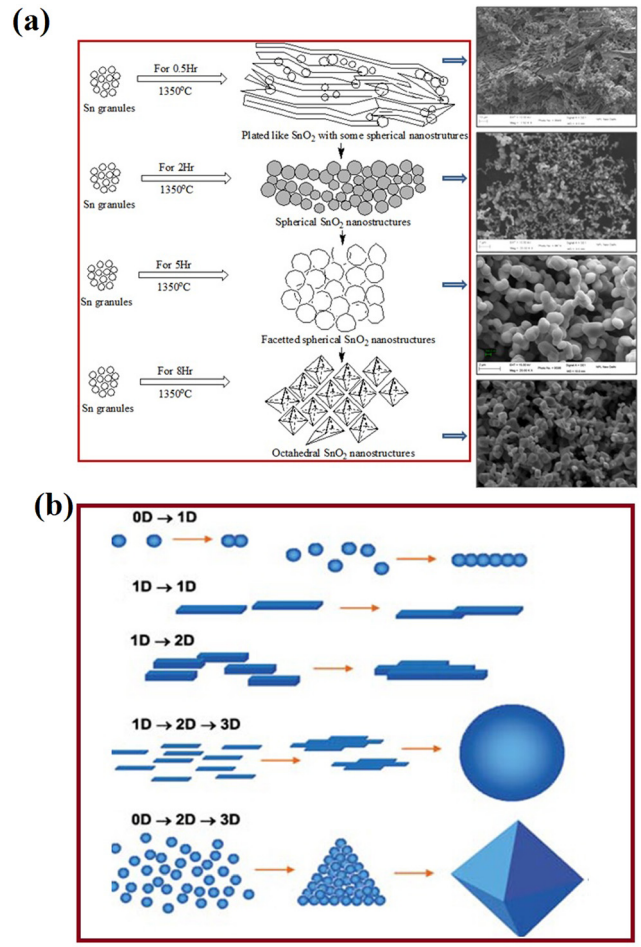

Fig. 7 (a) Schematic of the SnO_2 structural growth phenomena and morphological transformation with increasing evaporation time during thermal evaporation at 1350 °C. Reprinted with permission from ref. 152. Copyright 2014 Elsevier. (b) Various organizing schemes for the self-construction of nanostructures by oriented attachment. Reprinted with permission from ref. 151. Copyright 2004 John Wiley and Sons.

power consumption and high compatibility. The sensing properties are mostly influenced by the microstructure, surface modification by metal particles, and chemical composition of the materials. The environment conditions (temperature and relative humidity) are essential factors and matters of great concern for high-end sophisticated measuring and processing instruments in the storage and food sectors. The development and fabrication of humidity sensor devices based on new nanostructured materials are a continuously growing field for various applications. The sensing measurement results demonstrated that the water vapor in the air has a strong influence on the conductivity of the metal oxide nanostructure, and SnO_2 is one of the most suitable candidates for humidity sensing application. The SnO_2 nanostructures have also been widely used in humidity sensors. Due to the large band gap and low efficiency in the excitation and recombination process, SnO_2 has been used in numerous applications.[161–164] This extraordinary electron transition results in better sensing performance. The large surface-to-volume ratio and channel or network of the SnO_2 nanostructures offer enhanced sensitivity. Moreover, SnO_2 is an excellent material for the fabrication of solid-state gas sensors, and the long-term structural stability of SnO_2 nanostructures has been largely investigated for temperature-dependent metal oxide gas sensor operation.[164] Ultra-thin layers of SnO_2 and its integration with CMOS has been extensively applied for sensitive gas detection. SnO_2 nanostructures in the form of ultra-thin layers are used for the development of smart sensor devices, like CMOS integration of gas sensitive materials in daily life applications. The various aspects of thin layers of SnO_2 on CMOS chips have been studied for the technological importance of the devices and sensing performance.[162–164] The operating characteristics of the sensors are determined by both receptor and transducer functions, and consequently determines the efficiency of the chemical interaction and conversion into electric signals. Therefore, the morphology and crystallographic structure of the SnO_2 nanostructure are crucial properties for improving the performance of sensors. The recovery time, sensitivity, and reproducibility of the response of the sensors can be significantly increased or modified by the grain size, crystallinity, and morphology of the materials. The surface modification strategies, including doping states on the surfaces of the metal oxides, can be achieved by novel sol–gel, thermal evaporation and other synthesis methods. Moreover, the adsorption ability, sensitivity and catalytic activity also affect the sensor performance.[165–168]

3. Solar cell applications of metal oxide nanostructures

3.1 ZnO nanostructures-based solar cell

Sensitized solar cells (SSCs) provide a cheap, flexible and durable alternative to conventional silicon-based solar cells with reasonably high power conversion efficiencies.[169] ZnO nanostructures have been used as the photoanode. Various techniques have been used to increase the power conversion efficiency (PCE) of SSCs, such as optimizing the size of the nanorods and the crystallographic orientation.[170] Due to the n-type semiconductor property, high electron mobility, excellent photoluminescence, high conductivity, ease of fabrication and high thermal stability, ZnO has been extensively used in solar energy harvesting, especially in sensitized solar cells and heterojunction solar cells. Surface modifications in the ZnO nanostructure have been reported to tune the absorption spectra, and provide a high diffusion coefficient and electron mobility *via* the use of gold nanoparticles and doping with aluminium.[171,172] ZnO nanotubes have also been used as photoanodes, which showed increased PCE because of the higher surface area.[173,174] Since ZnO is not compatible with the most commonly used Ru-based dyes,[175] metal-free dyes[176–178] have been used to increase the PCE of ZnO-based solar cells to >5%. Doping of ZnO thin films with various elements such as iodine has been also utilized to further increase the PCE of solar cells to beyond 20%.[179] Furthermore, ZnO nanostructures have been used in perovskite-sensitized solar cells as an electron

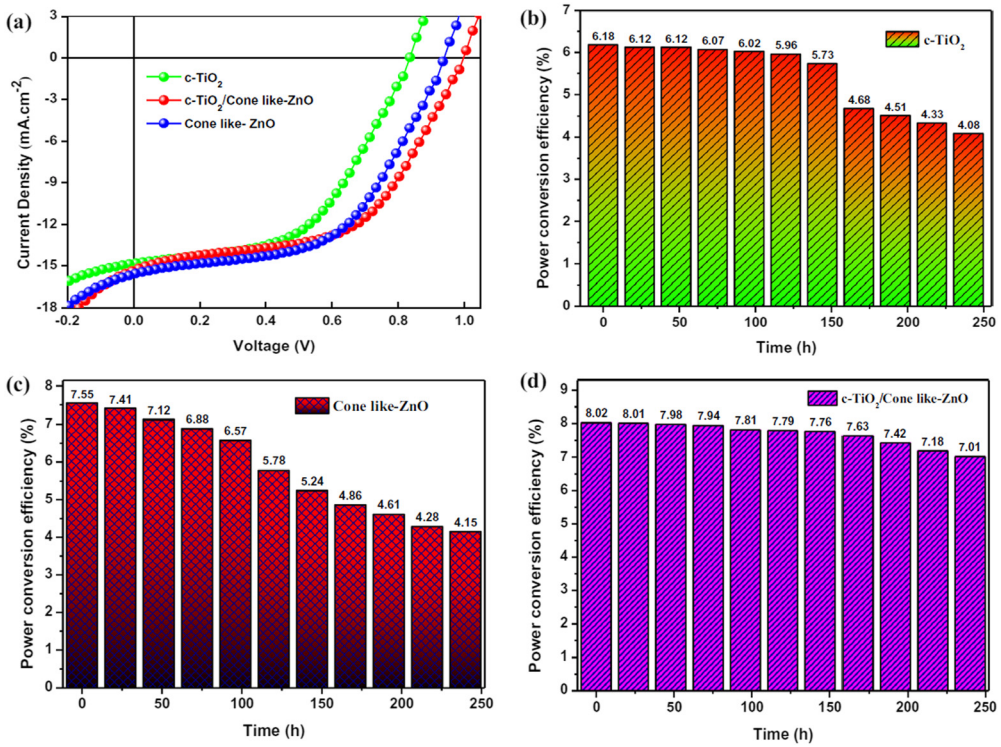

Fig. 8 Use of cone-like ZnO improves the perovskite solar cell performance. (a) Better *J*–*V* characteristics of upon addition of the cone-like ZnO as a part of ETL. (b–d) PCE over time for the single layer c-TiO_2, cone-like ZnO and bilayer of c-TiO_2 with come like ZnO as ETL. Reprinted with permission from ref. 180. Copyright 2021 Springer Nature.

transport layers (ETL) for interfacial engineering to enhance the device performance (Fig. 8). Incorporation of cone-like ZnO with the c-TiO_2 as a part of ETL improves the charge transfer at the ETL-perovskite interface, and also leads to a reduction in the recombination losses. This led to better *J*–*V* characteristics (Fig. 8(a)) and higher PCE for c-TiO_2 and the cone-shaped ZnO bilayer ETL (Fig. 8(b–d)). This bilayer also had the lowest reduction in PCE (device degradation) as a function of time, highlighting the importance of ZnO in improving the device stability by suppressing the chemical reactions at the ETL-perovskite interface.[180]

It has been reported that the morphology of ZnO also plays a significant role in improving the PCE efficiency, and ZnO nanoparticles exhibit better efficiencies than nanorods as the 1D structures provide direct electron pathways for electron transport.[181] The electrons suffer several trapping and detrapping events, especially at the grain boundaries of nanoparticles.[182,183] Doping in ZnO can also increase the PCE of solar cells by multiple ways, such as by increasing the carrier concentration, carrier mobility and conductivity, while reducing the internal resistance, and promoting electron extraction from the perovskite layer.[184,185] Fig. 9 summarizes the key application areas of nanostructured ZnO in solar cells.[186]

It was observed that depending on the doping elements, the morphologies of the ZnO nanostructure changed. This resulted in the interface interaction between the perovskite and ZnO nanostructure increasing, causing the work function to decrease, which facilitated the easier extraction of an electron

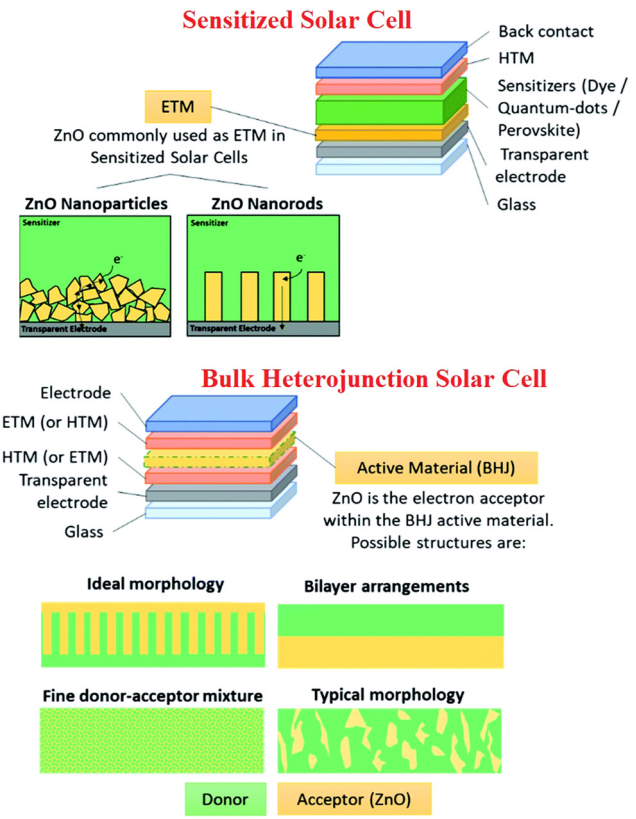

Fig. 9 Application of the ZnO-nanostructured solar cell. Reprinted with permission from ref. 186. Copyright 2020 Royal Society of Chemistry.

into the ZnO layer.[187,188] Using the doping methodology in ZnO, solar cells with PCE >21% have been fabricated.[189] The PCE of these SSCs depends on the number of free electrons, back transfer of electrons from ZnO, and the total surface area of ZnO. In heterojunction solar cells, ZnO is used as an n-type semiconductor in the active layer,[190,191] an electron transport,[192,193] or a buffer layer.[194] However, the solar cells required more optimization to improve the power conversion efficiencies compared to conventional solar cells. In the organic solar cells, ZnO has also been used as a cathode buffer layer where power conversion efficiencies as high as 15.7% have been observed.[195] ZnO nanostructures have also been used as a part of the anti-reflection layer in CSZTe and Si solar cells, leading to a reduction in the reflection from 7.76% to 2.97%.[196,197] Further enhancements in the performance of the ZnO nanostructures-based solar cells can be made by increasing the surface area, which can allow for increased rate of kinetics during solar cell functioning, and by enhancing the light absorption capability.

3.2 SnO_2 nanostructures-based solar cell

Due to the large bandgap, good transparency in the optical spectrum, low refractive index, and high stability, SnO_2 nanostructures have been extensively used for solar energy-harvesting applications.[198] Various nanostructures of SnO_2 have also been used to fabricate the solar cell. In particular, SnO_2 nanowires with few defects such as grain boundaries have been used to fabricate the dye-SSCs, as well as perovskite solar cell PSCs.[199–201] Very high PCEs of 14.2% were obtained from the SnO_2-based nanowires-based solar cells.[202] Nanorods have an open porous structure, which allows for more efficient filling by the perovskite crystals, leading to enhanced light absorption[203,204] and PCE of 18.7% from the solar cells.[205] SnO_2 nanotubes with high electrical conductivity are also used to fabricate the solar cell, and an efficiency of about 12.1% has been achieved.[206] The SnO_2 nanosheets used to promote the interfacial charge transfer was used to fabricate the solar cell. The nanosheets showed high photo-induced carrier collection,[207,208] and a very high PCE of 18.3% was reported.[209] The performance of the solar cell was also achieved by passivation of the SnO_2–pervoskite interface to suppress defects, such as Sn interstitials, O vacancies, and film cracking, which would degrade the device performance.[210,211] Various strategies, such as doping with metals and halogens (which also improves the energy level alignment[212–214]), bilayer ETLs using various oxides,[215–217] interface modification with ammonium salts,[218,219] and quantum dots[220] have been employed to suppress these defects and increase the PCE of the solar cell. The highest PCE using SnO_2 in a perovskite solar cell has been reported to be 25.2%. The SnO_2-based perovskite solar cell showed longer durability compared to the TiO_2-based perovskite solar cell.[221–223] Fig. 10 (inset) shows a schematic of a perovskite solar cell fabricated with a hybrid ETL of mesoporous TiO_2/amorphous SnO_2 (mp-TiO_2/a-SnO_2). As can be seen in Fig. 10, the a-SnO_2 addition leads to reduced hysteresis in the *J–V* curve because of a better bandgap alignment, which leads to the fast electron extraction from the perovskite. This also leads to a reduction in the nonradiative

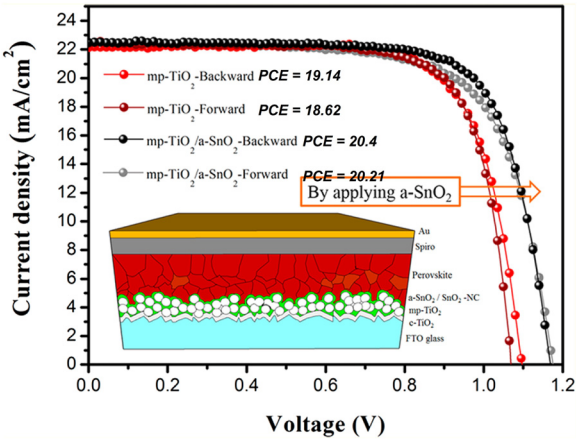

Fig. 10 Cross-sectional SEM image of the perovskite solar cell based on mp-TiO_2/a-SnO_2. *J–V* curves for mp-TiO_2 and mp-TiO_2/a-SnO_2 along with the power conversion efficiencies. Inset shows a schematic of a perovskite solar cell based on mp-TiO_2/a-SnO_2. Reprinted with permission from ref. 227. Copyright 2018 American Chemical Society.

carrier recombination, which improves the V_{OC} by ~170 mV and PCE of mp-TiO_2/a-SnO_2 by ~1.5%. It has also been reported that the addition of a mp-SnO_2 layer instead of a planar SnO_2 ETL layer acts as an energy bridge by facilitating energy transfer from perovskite to SnO_2, and also increases the contact area for more efficient extraction. This leads to lower hysteresis losses and higher PCE with mp-SnO_2, as compared to that with planar SnO_2, as can be seen in Fig. 11a. Moreover, mp-SnO_2 inhibits degradation of perovskite and prevents the penetration of harmful substances, such as moisture, oxide or gold into the perovskite layer, leading to much better stability and lower degradation of PCE over time (Fig. 11b).[224] Because of its low temperature processability and stability, SnO_2 has sparked a lot of interest as ETL for flexible perovskite solar cells.[224–226] However, controlling the processing temperature and crystallinity defects is required to fabricate high-performance SnO_2-based flexible devices.

4. Biological applications

4.1 Antimicrobial application of ZnO nanostructures

ZnO nanoparticles (NPs) possess unique physicochemical and structural properties, including shape, particle size, zeta potential, crystallinity and porosity, which make them attractive as antimicrobial agents. ZnO NPs show effectiveness against different types of microbes, fungi, viruses, and Gram-positive and Gram-negative bacteria.[228] In one study, Faisal *et al.*[229] synthesized ZnO NPs from the fruit extract of *Myristica fragrans*, which function as a reducing, capping and stabilizing agent for NPs. Their antibacterial activity against bacterial species, such as *E. coli*, *P. aeruginosa*, *K. pneumoniae* and *S. aureus*, was analyzed.[229] The obtained results indicate that the maximum zone of inhibition (ZOI) was displayed when these NPs were treated with *K. pneumoniae*, with 27 ± 1.73 mm as compared to 15 ± 1.54 mm, 17 ± 1.66 mm and 21 ± 1.73 mm for *E. coli*,

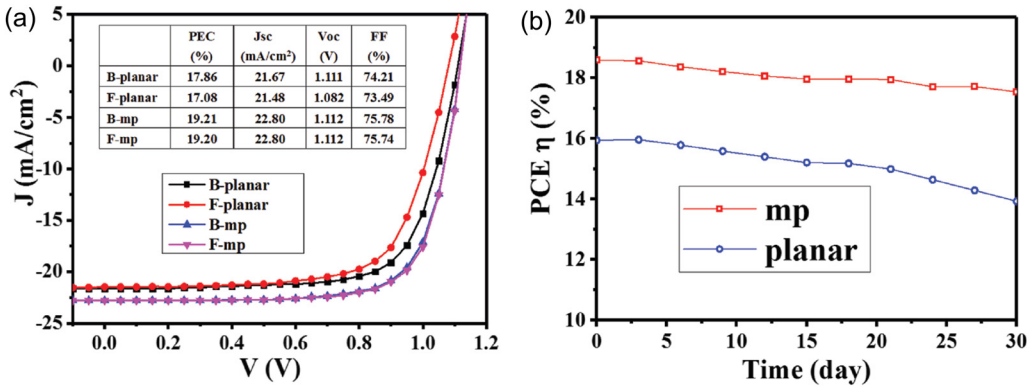

Fig. 11 (a) J–V graphs obtained of the planar SnO_2 and mp SnO_2 PSCs from under backward and forward voltage scanning. (b) PCEs of the planar SnO_2 and mp SnO_2 PSCs monitored every 3 d; the measurement was performed under AM 1.5G with input solar power P_{in} of 100 mW cm^{-2}. Reprinted with permission from ref. 224. Copyright 2018 John Wiley and Sons.

P. aeruginosa and *S. aureus*, respectively. The authors suggested that bioactive compounds present in the plant-mediated synthesis process possess therapeutic activities.[228a]

The widely accepted plausible mechanism is that the generation of the reactive oxygen species (ROS) is responsible for the antibacterial action of ZnO NPs. ROS can break the chemical bonds of the organic matter present in bacteria, and cause a bactericidal effect (Fig. 12).[228b] Moreover, nano-sized particles release metal ions that can lead to cell content leakage, lipid peroxidation, oxidative stress, cytoplasm leakage, protein denaturation and DNA damage.[230–232] It has also been reported that ZnO NPs show efficacy against bacterial species in the dark, and it is more significant at low bacterial concentration. In a dark environment, some additional mechanisms might take part, such as the release of Zn^{2+} ions penetrating the bacterial moiety, causing protein denaturation and cellular respiratory disorder (Fig. 12b).

When communities of bacteria adhere to the surface and are embedded in extracellular polymeric substances (EPS), they form a biofilm. The bacterial biofilm is highly resistant to any antibiotics or traditional biocidal drugs. Different types of biofilms are formed in wound beds, and therefore complicate the wound healing process. ZnO NPs have shown improved antimicrobial properties against planktonic bacteria and bacterial biofilms. Rayyif *et al.*[233] found ZnO NPs-coated polyester-nylon wound dressings to be effective against planktonic (Gram-positive and Gram-negative) and biofilm-embedded bacterial strains. Bacterial viability was analyzed in a time- and dose-dependent manner. For Gram-positive bacteria (*S. aureus* and *E. faecalis*), substantial viability loss was observed at least at 12 h of incubation, which was higher than that of the case of Gram-negative bacteria. Viability loss was 6 h of incubation for the strains of *P. aeruginosa* and *E. coli*. The difference in their viability loss was related to their cell wall composition, as Gram-positive bacteria possess a thick peptidoglycan cell wall. Thus, the Gram-negative bacterial cell wall was more susceptible to be pierced by ZnO NPs. Biofilm inhibition was observed at 48 h for *S. aureus*, *E. faecalis*, and *E. coli* at 0.6 and 0.9% ZnO-coated dressings, while the *P. aeruginosa* biofilm was observed to be reduced after 72 h of incubation. Thus, ZnO-based dressings could be effectively used to deal with chronic wounds.

Moreover, ZnO nanostructures were observed to be effective against many viruses, such as herpes simplex virus type 1 (HSV-1),[234,235] Hepatitis A virus (HAV),[236] human metapneumovirus,[235] and a virus from the *Coronaviridae* family.

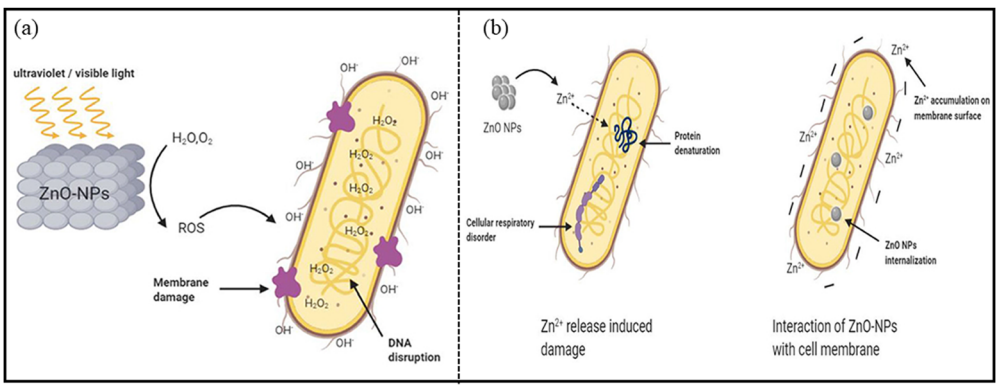

Fig. 12 Antibacterial mechanism of ZnO NPs through (a) ROS production, causing a bactericidal effect, (b) Zn^{2+} ions release in a dark environment. Reprinted with permission from ref. 228*b*. Copyright 2020 Frontiers.

Billions of people worldwide were infected through a severe acute respiratory syndrome coronavirus 2 (SARS-CoV-2). The WHO declared the virus outbreak as a Public Health Emergency of International Concern as it is a pandemic threat. SARS-CoV-2 has morphological similarity with NPs, as it is an enveloped virus with particle-like features and possesses a radius in the range of 30–70 nm.[237] Thus, NPs have immense potential to mimic and tackle this virus.

Firstly, it is necessary to gather information about the structural proteins present in the SARS-CoV-2 protein. SARS-CoV-2 is a single-stranded and enveloped ribonucleic acid virus. As shown in Fig. 13a, the spike surface glycoprotein (S), matrix protein (M), small envelope protein (E), and nucleocapsid protein (N) are the four structural proteins of SARS-CoV-2. The U.S. National Institute of Allergy and Infectious Diseases (NIAID) has released electron micrographs revealing the morphology of SARS-CoV-2, as shown in Fig. 13(b–e).[238]

Tavakoli *et al.*[235] demonstrated the antiviral activity of ZnO NPs and PEGylated ZnO NPs (polyethylene glycol-coated ZnO NPs) against HSV-1. The authors reported that after coating the NPs with PEG, the antiviral activity was improved compared to only ZnO NPs at the same concentration. That may be due to less agglomeration by surface coating these NPs with PEG, and it could be considered as an effective agent for enhancing antiviral activities. Generally, the reason why ZnO NPs possess potency against many viruses could be that Zn has antiviral activity, and thus it can (i) prevent the entry of the virus, (ii) prevent the replication of the virus, and (iii) trigger ROS, which lead to oxidative injury and cell death.

Similarly, Attia *et al.*[236] investigated the antiviral activity of ZnO NPs of 20–30 nm size (estimated by TEM) against HAV with 58.83% at the maximum non-cytotoxic concentration. However, the authors have not mentioned the plausible mechanism behind it.

4.2 Antilarvicidal activity of ZnO nanostructures

Mosquitoes, such as *Aedes aegypti* and *Aedes albopictus*, are the primary vector to transmit the deadly disease, dengue. Not only dengue, but yellow fever, Chikungunya, and Zika virus are also transmitted by these mosquitoes. Malaria is the prevalent mosquito-borne disease that is caused by *Anopheles*. To combat these deadly diseases, nanotechnology plays a very important role. ZnO nanostructures are known to control these vector mosquitoes due to its impressive physico-chemical properties. The possible mechanism is that ZnO NPs get accumulated in the thorax and abdomen in the larvae of mosquitoes, such as *Aedes aegypti*. However, there is still no clarity about the morphology of ZnO NPs. To study this, Gunathilaka *et al.*[239] synthesized different morphologies of ZnO, such as star-, needle-, plate- and cubic-shaped, using the chemical route of synthesis to check their larvicidal properties on *Aedes albopictus* and *Anopheles vagus*. The LC_{50} value was considered as the measure of the toxic effect on mosquitoes. It was observed that among the different morphologies, the star-shaped one showed higher toxic effects against both mosquito larvae. The lowest values of LC_{50} were 38.90 mg l^{-1} and 4.78 mg l^{-1} against *Aedes albopictus* and *Anopheles*, respectively. However, the plate-shaped morphology displayed the least toxic effect to the larvae at 68.38 mg l^{-1} and 10.47 mg l^{-1} for both *Aedes albopictus* and *Anopheles*, respectively. From Fig. 14a, it was confirmed that the star- and needle-shaped NPs cause death to a greater proportion of both types of larvae compared to the cubic- and plate-shaped NPs. The authors explained that the possible reasons could be as follows: (i) different morphologies possess different

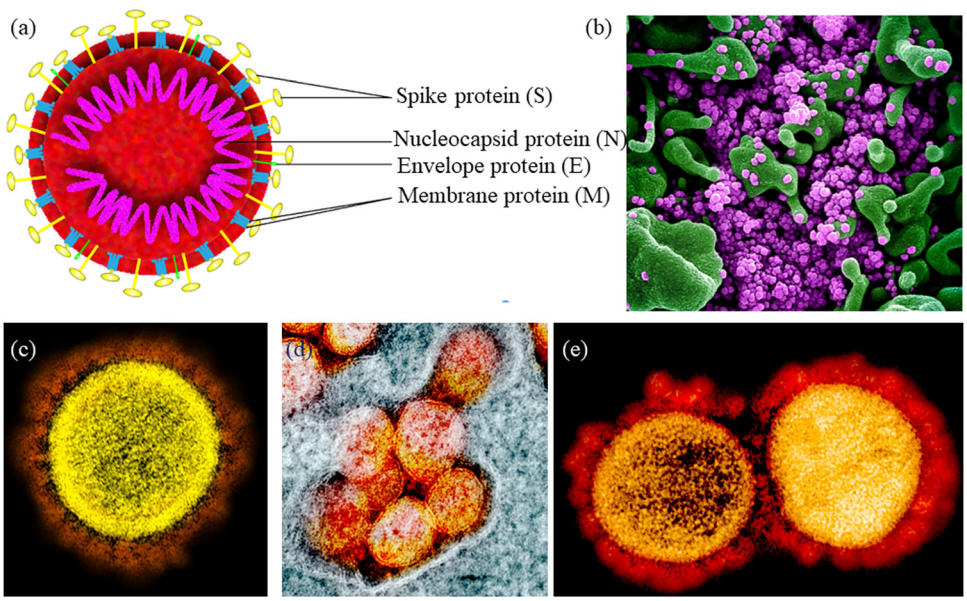

Fig. 13 (a) Structure of SARS-CoV-2. Reprinted with permission from ref. 238. Copyright 2020 Elsevier. (b) Scanning electron microscopy (SEM) image showing SARS-COV-2 virus particles (purple) in apoptotic cell (green). (c–e) Transmission electron micrograph (TEM) of SARS-CoV-2 virus particles, isolated from a patient. (b–e) Photo Credit: NIALID.

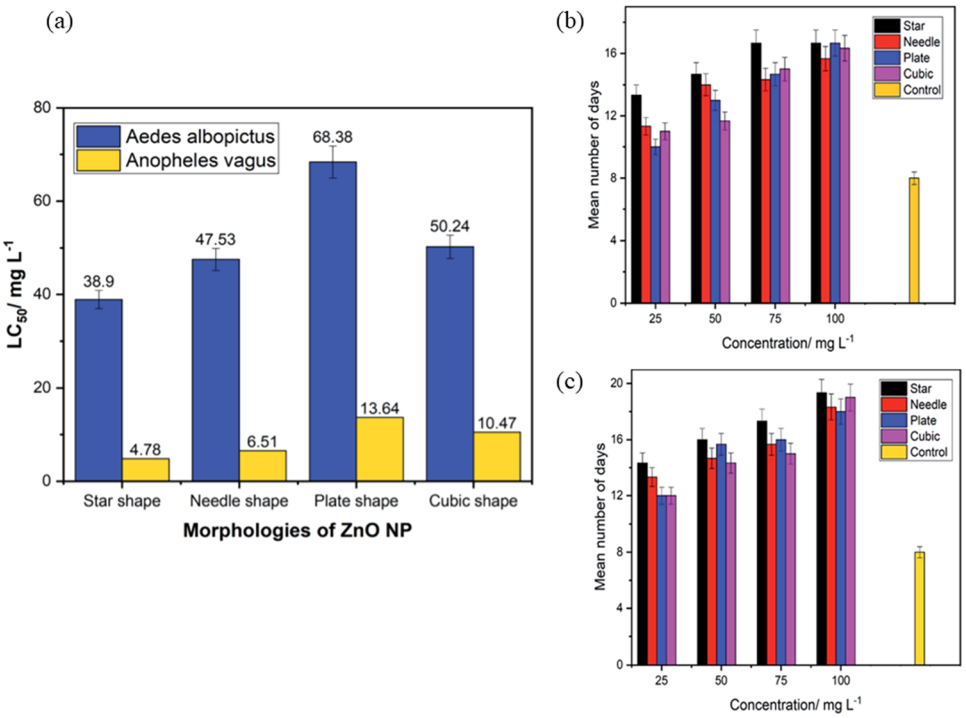

Fig. 14 (a) The LC_{50} values against the larvae of *Aedes albopictus* and *Anopheles vagus* mosquitoes obtained from the four different morphologies of ZnO nanoparticles. (b and c) Number of days needed by the mosquito larvae to complete the life cycle under exposure to various morphologies and concentrations of ZnO nanoparticles. (b) *Aedes albopictus*, (c) *Anopheles vagus*. Reprinted with permission from ref. 239. Copyright 2021 Royal Society of Chemistry.

active facets. The facets provide a high surface-to-volume ratio, as well as a large number of polar surfaces to trap oxygen molecules that enhance the larvicidal activity. (ii) The star-shaped structure has spikes in a random orientation, causing more destruction to the larval body. Mosquito larvae, after exposure to ZnO nanostructures for 24 h, were continuously monitored for 21 days to test the development of the surviving larvae. The dose-dependent results of ZnO nanostructures are shown in Fig. 14(b and c). In the control, the larvae emerged as adults within 8 ± 1 days. However, the larvae exposed to the highest concentration of ZnO required a long time to complete its life cycle, thus confirming that ZnO has an impact on the rate of growth of the mosquito vector.

Similarly, Dhavan *et al.*[240] analyzed ZnO nanorods synthesized by green method to evaluate the larvicidal activity against the dengue vector. The LC_{50} value of 24.74 μg ml^{-1} proved that the rod-like morphology is also effective against *Aedes aegypti*. One of the mosquito larvae, *Culex tritaeniorhynchus*, extracts blood from humans as well as animals. The efficacy of ZnO NPs was studied against this larva by Velsankar *et al.*[241] The results indicate that the mortality rate was initiated at 12 h for 40 ppm concentration of NPs. The great larvicidal activity was noticed at the lowest concentration of ZnO. It has been reported that ZnO NPs are accumulated and deposited in different parts of the larval body, such as the respiratory region, causing suffocation, and the alimentary canal, causing tissue layer damage. Zn^{2+} ions also hinder the growth of larvae.

4.3 Anticancer activity of ZnO nanostructures

Cancer, the abnormal growth of tissues, caused the death of around 10 million people in 2020. The most common cancers include lung cancer (1.80 million), colon and rectum (935 K), liver (830 K), stomach (769 K) and breast cancer (685 K), as per recent projections by the World Health Organization (WHO) (**https://www.who.int/news-room/fact-sheets/detail/cancer**). Traditional approaches, such as chemotherapy and radiotherapy, possess substantial side effects such as immunosuppression. They also affect normal cells, cause anemia, or in even more severe cases, lead to death. To overcome such drawbacks, nanotechnology plays a very crucial role. ZnO NPs are not only effective against cancer diagnosis, but they show efficacy against cancer cells. ZnO NPs have been reported to produce ROS upon contact with the cells, causing cell death to cancer tissues. It has been shown that ZnO NPs obtained from plant- and microbes-mediated synthesis show good anticancer activities. Moghaddam *et al.*[242] affirmed that ZnO NPs obtained from a new strain of yeast, *P. kudriavzevii*, have powerful efficacy against breast cancer cells. The viability of the cancer cells was concentration-dependent, and decreased with increasing ZnO NPs concentration. The value of IC_{50} for ZnO NPs at 24 h was estimated to be 121 μg ml^{-1}. The authors claimed that the loss of viability occurs by inducing sub-G1 phase apoptosis, and upregulating pro-apoptotic genes, *e.g.*, p21, p53, JNK, Bax, and downregulating anti-apoptotic genes like Bcl-2, ERK1/2 and AKT1. Similarly, fabricated ZnO NPs from *P. Chrysogenum*

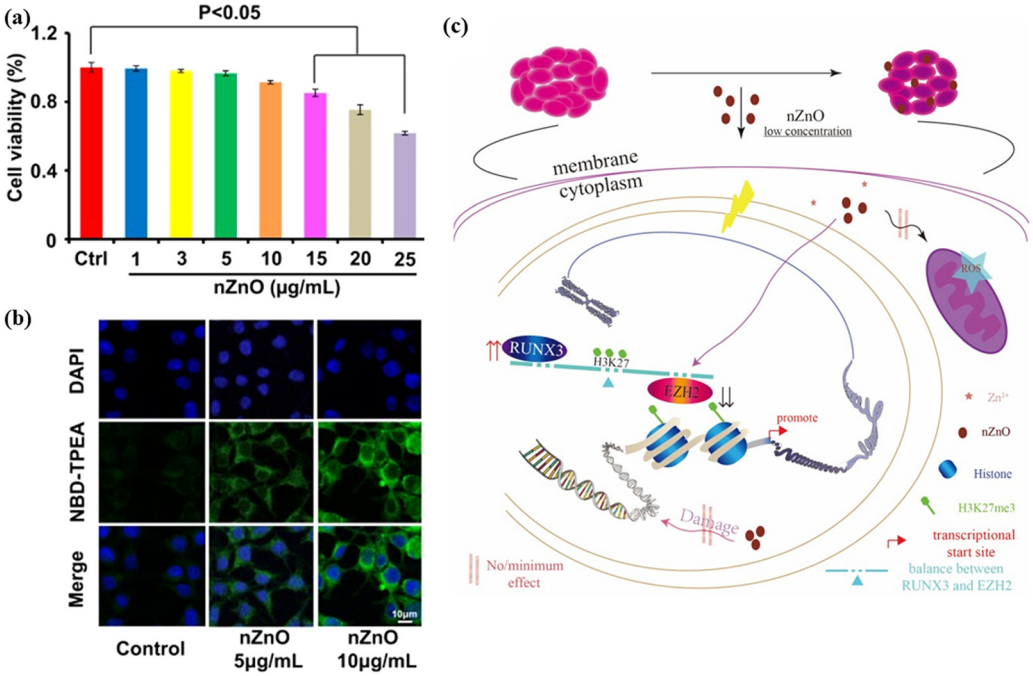

Fig. 15 (a) Zinc detection and cytotoxicity assessment in T24 cells by ZnO NPs treatment. (b) Confocal images [NBD-TPEA (green) and DAPI (blue) staining] for the intracellular zinc ion in T24 cells upon ZnO NPs exposure for 2 days. (c) A schematic image shows the epigenetic mechanism underlying the n-ZnO-mediated anticancer effect in T24 cells. Reprinted with permission from ref. 244. Copyright 2020 Dove Press.

demonstrated anticancer activity against breast and colon cancers. The authors reported that on irradiating the NPs with gamma radiation, the performance against the cancer cells increased.[243] Recently, Zhang *et al.*[244] studied the cytotoxic effect of ZnO NPs against human bladder cancer cell lines, T24. At low NPs concentrations, 15 μg ml^{-1}, ZnO did not show any substantial effect after 48 h of exposure, as shown in Fig. 15. When confocal microscopy was used to investigate the level of zinc ion, green fluorescence was observed to increase with increasing NPs concentration. The NPs concentration of 10 μg ml^{-1} exhibited higher fluorescence intensity than that at 5 μg ml^{-1} (Fig. 15(b)). Upon further investigation, it was confirmed that a low dose of ZnO NPs induces S phase arrest and late apoptosis in T24 cells. In addition, it inhibited cellular migration and aggressive capacity because of the histone methylation change. The plausible mechanism of ZnO at low concentration in restraining bladder cancer proliferation and migration in T24 cells is shown in Fig. 15(c).

4.4 Antimicrobial action of SnO_2 nanostructures

SnO_2 nanostructures exhibit antimicrobial property against a wide range of microbes, such as bacteria (both Gram-positive and -negative), viruses, and fungi, owing to their large surface area. The antimicrobial action of the nanostructures depends on a number of factors: (i) synthesis route, (ii) morphology of NPs, (iii) particle size of NPs, (iv) concentration of NPs and (v) nature of the capping agent, if used while fabricating NPs. It has been reported in the literature that SnO_2 nanostructures fabricated through green methods are much preferred for their antimicrobial activities.[245] Briefly, green methods utilize plant-, bacteria-, and protein-extracts to synthesize different morphologies of nanoparticles (NPs). Through this method, stable and high yield products are produced, and the starting materials are eco-friendly and biocompatible.[228] Thus, the obtained nanostructures from this way are more biocompatible to be used for biological applications. Moreover, the extract used for green synthesis acts as a capping/stabilizing agent, leading to the prevention of aggregation, and therefore improves the biological potential of NPs.[246] Vidhu and his team[247] fabricated SnO_2 nanoparticles by *Saraca indica* flowers, and showed their antibacterial activity against *E. coli* bacteria. The authors revealed that the plausible mechanism behind the antibacterial action is the generation of reactive oxygen species (ROS) NPs. The produced ROS interact with the bacterial cell membrane and penetrate the cell, as shown in Fig. 16. This results in bacterial cell death. In another study by Ayeshamariam *et al.*,[248] synthesized SnO_2 NPs by *Aloe Vera* plant extract were observed to be effective against both Gram-positive (*S. aureus*, *S. typhi*, *S. pyogenes*) and Gram-negative (*E. coli* and *P. aeruginosa*) bacteria, as analyzed *via* well diffusion method. The zone of inhibition (ZOI) was calculated by measuring the diameter of the inhibition zone around the well, including the well diameter. A greater value of ZOI indicates effective inhibition property. The authors reported on 100% and 75.9% activity against Gram-negative and Gram-positive isolates, respectively. The reason behind this was the presence of an *Anthraquinones* component possessing antimicrobial activity, as mentioned by the authors. Vidhu *et al.*[247] also revealed that as the concentration of NPs increased, the bactericidal effect was also enhanced.

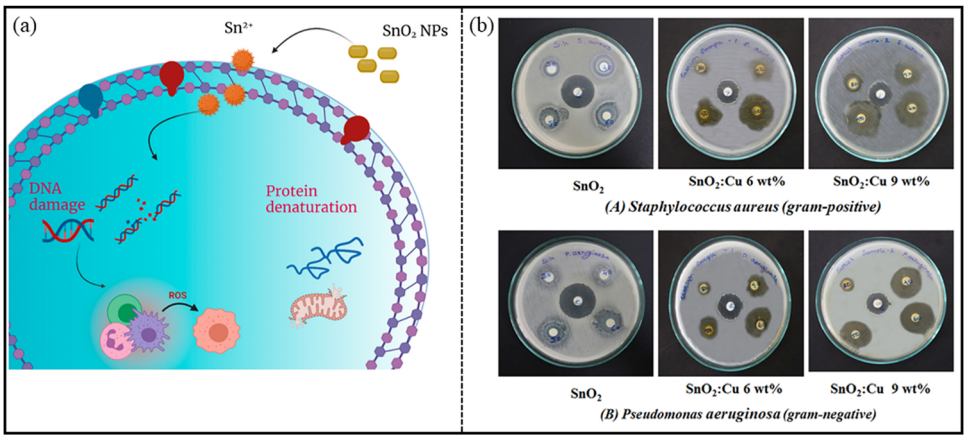

Fig. 16 (a) Possible mechanism of the antibacterial action of SnO_2 NPs. Reprinted with permission from ref. 251. Copyright 2021 MDPI. (b) Antibacterial activity of the pure and Cu-doped SnO_2 NPs: (a) SnO_2, (b) SnO_2:Cu, 6 wt%, (c) SnO_2:Cu, 9 wt%. Reprinted with permission from ref. 250. Copyright 2020 Elsevier.

It has also been reported in the literature that transition metal ions-doped SnO_2 show potent antimicrobial activity, such as Co-doped, Ag-doped, Ce-doped, Cu-doped SnO_2 NPs. Bhawna *et al.*[249] reported on the activity of cerium (Ce)-doped SnO_2 NPs against *E. coli* bacteria. At low concentrations of 0.25–3 mg of NPs, no antibacterial activity was observed. However, on increasing the concentration to 4–5 mg, the antibacterial activities were analyzed by estimating the diameter of ZOI. Similarly, Sathishkumar *et al.*[250] reported on the enhanced antibacterial activity of Cu-doped SnO_2 NPs compared to pure SnO_2 NPs, as revealed by calculating the ZOI (Fig. 16(b)). The authors claimed that less inhibition zone in the case of SnO_2 NPs was probably due to the greater particle size and low release of Sn^{4+} ions, generating less ROS. On increasing the Cu dopant concentration, the diameter of the inhibition zone increased against both types of bacteria (*P. aeruginosa* and *S. aureus*) because of the improved rate of generation of Cu^{2+} ions and Sn^{4+} ions, as well as larger surface area.

Khan *et al.*[252] analyzed the impact of green synthesized un-doped SnO_2 NPs, Co-doped SnO_2 NPs and plant extract on the viability of bacterial strains such as *E. coli* and *B. subtilis via* confocal and electron microscopy. Confocal micrographs (Fig. 17(a))

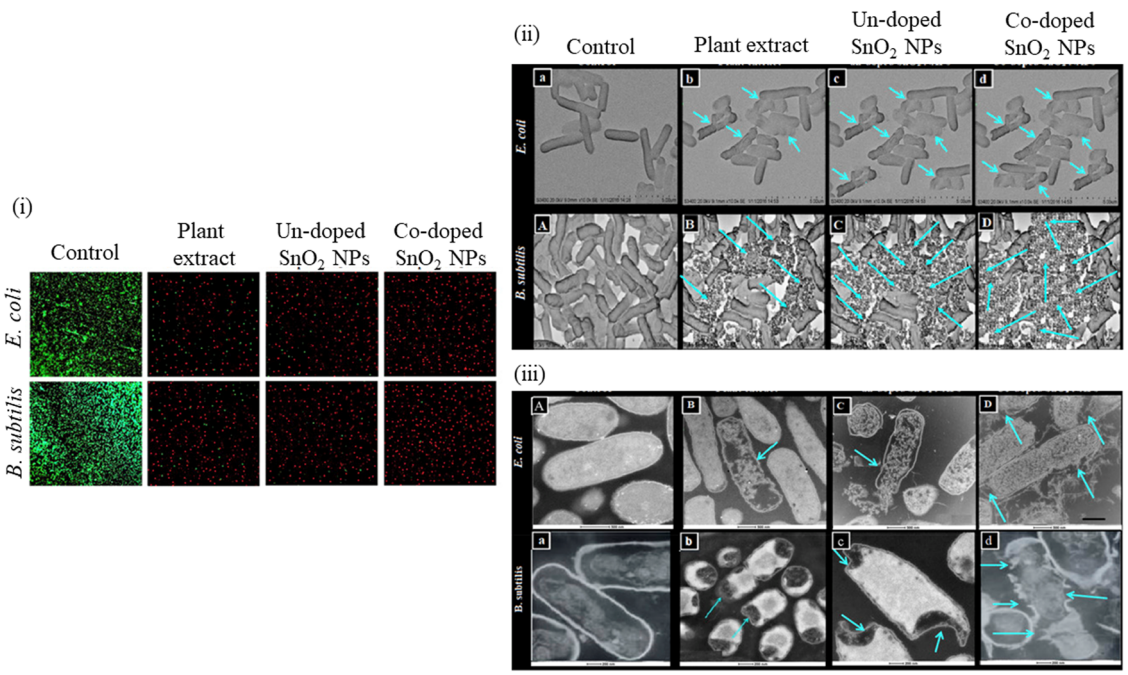

Fig. 17 The measured confocal images (i), produced by the control and treated *E. coli* and *B. subtilis* with plant extract, green synthesized un-doped SnO_2 NPs and co-doped SnO_2 NPs. Morphology of the untreated and treated *E. coli* and *B. subtilis* cell strains. TEM images (ii, iii) of the untreated and treated *E. coli* and *B. subtilis* strains, *i.e.*, control, plant extract, un-doped SnO_2 NPs and Co-doped SnO_2 NPs (A–D) and (a–d), respectively. Reprinted with permission from ref. 252. Copyright 2018 Elsevier.

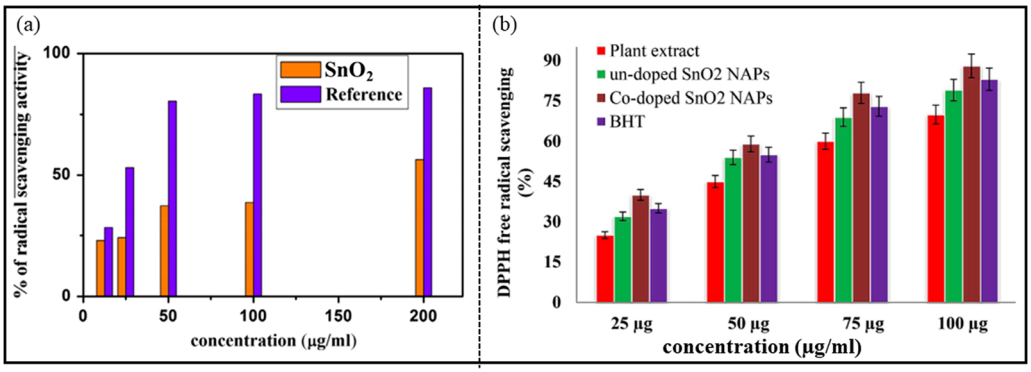

Fig. 18 Antioxidant activity using DPPH assay: (a) SnO_2 NPs. Reprinted with permission from ref. 247. Copyright 2015 Elsevier. (b) Plant extract, green synthesized un-doped SnO_2 and Co-doped SnO_2 NPs, employing BHT as an external standard. Reprinted with permission from ref. 252. Copyright 2018 Elsevier.

show the dead and live bacterial cells in red and green color, respectively. The results indicated that when bacterial cells were exposed to Co-doped SnO_2 NPs, they were observed to be 100% dead compared to the untreated bacterial cells treated with plant extract and un-doped SnO_2 NPs. Co-doped SnO_2 NPs demonstrated almost 99% red fluorescence, confirming dead cells as shown in (Fig. 17(b)). The results were found to be in agreement with SEM (Fig. 17ii) and TEM micrographs (Fig. 17(c)). In the control samples of *E. coli* and *B. subtilis*, the morphology of these bacteria is very distinct and continuous. However, their morphologies were observed to be disordered when these bacterial cells were treated with plant extract and un-doped SnO_2 NPs. The authors also observed that the bacterial membrane disruption was higher when treated with Co-doped SnO_2 NPs than when treated with plant extract and SnO_2 NPs, as revealed by SEM and TEM. Significant and extraordinary cell death of the bacteria was noticed by the Co-doped SnO_2 NPs.

In addition to being effective against bacteria, Co-doped SnO_2 NPs synthesized by green route were found to be effective against different fungal strains, such as *A. flavus, A. niger*, and *C. albicans*, with a high ZOIs of 23 ± 0.08 mm, 17 ± 0.04 mm, and 26 ± 0.06 mm, respectively. The authors suggested that its effectiveness was due to the Co doping, greater grain size and surface area, and thus more antifungal propensity.[252] Similarly, in another report by Ayeshamariam *et al.*,[248] SnO_2 NPs of around 100 nm size showed antifungal activity for *A. niger* and *M. indicus*. The SnO_2 nanostructures are observed to be effective as antiviral agents. Trigilio *et al.*[253] demonstrated the antiviral activity of SnO_2 nanowires, with the length varying from a few mm to 1 cm, and the diameters ranging from a few nm to the mm scale. These nanowires act like a natural target by showing an ability to compete for the virus at the attachment

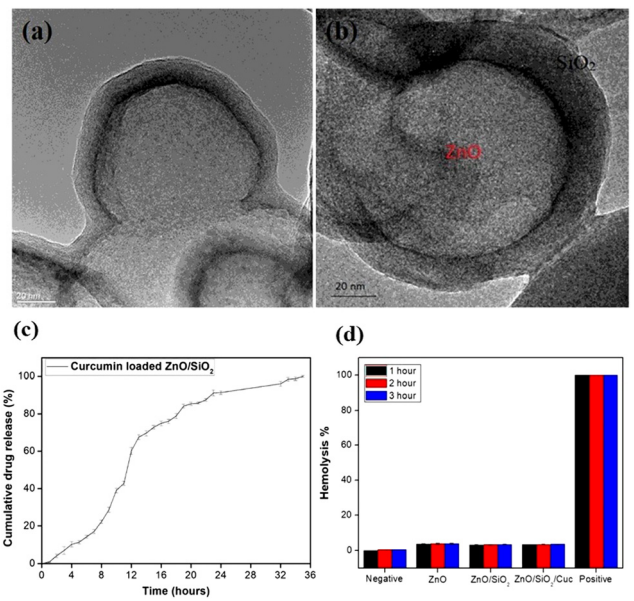

Fig. 19 (a and b) HRTEM image of the ZnO/SnO core shell nanoparticles. (c) Drug release profile of the curcumin-loaded ZnO/SnO_2 core shell structure, and (d) hemolysis percentage of the pure and ZnO/SnO_2 core shell nanoparticles. Reprinted with permission from ref. 259. Copyright 2020 Springer Nature.

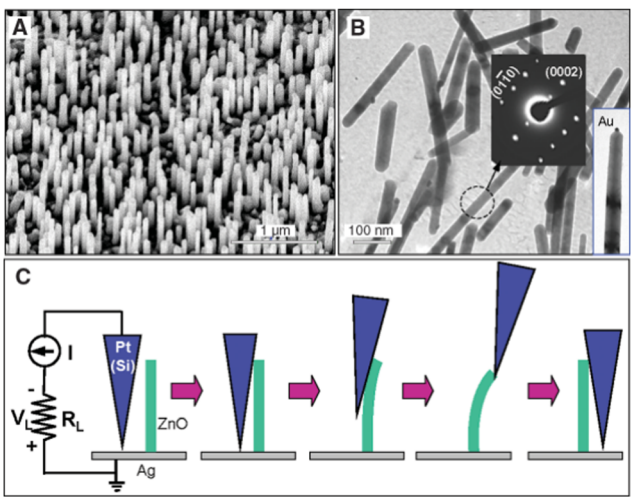

Fig. 20 (a and b) TEM image of the vertically aligned ZnO nanowires. (c) Schematic of the AFM measurement of single ZnO nanowires for piezoelectric measurements. Reprinted with permission from ref. 271. Copyright 2006 The American Association for the Advancement of Science.

step. The authors reported that at the concentration of 500 and 1000 μg ml^{-1}, the Herpes simplex virus type 1 (HSV-1) entry was 5 times lower than untreated cells.

4.5 Antioxidant activity of SnO_2 nanostructures

Antioxidants play a very important role in protecting the human body from free radical damage. Actually, when biomolecules present in the human body interact with oxygen, they produce free radicals. Free radicals cause degradation to biomolecules. Thus, the function of antioxidants is to scavenge the free radicals, thereby terminating the oxidative harm to the human body. SnO_2 NPs show good antioxidant property by scavenging 1,1-diphenyl-2-picrylhy-drazyl (DPPH) free radicals. Generally, the antioxidant capacity is enhanced with the increase in the concentration of SnO_2 NPs. Hong *et al.*[254] determined the inhibition of DPPH free radicals by SnO_2 NPs synthesized by means of *Litsea cubeba* fruit extract, with the half maximal inhibitory concentration (IC_{50}) value to be 2257.4 μg ml^{-1}.

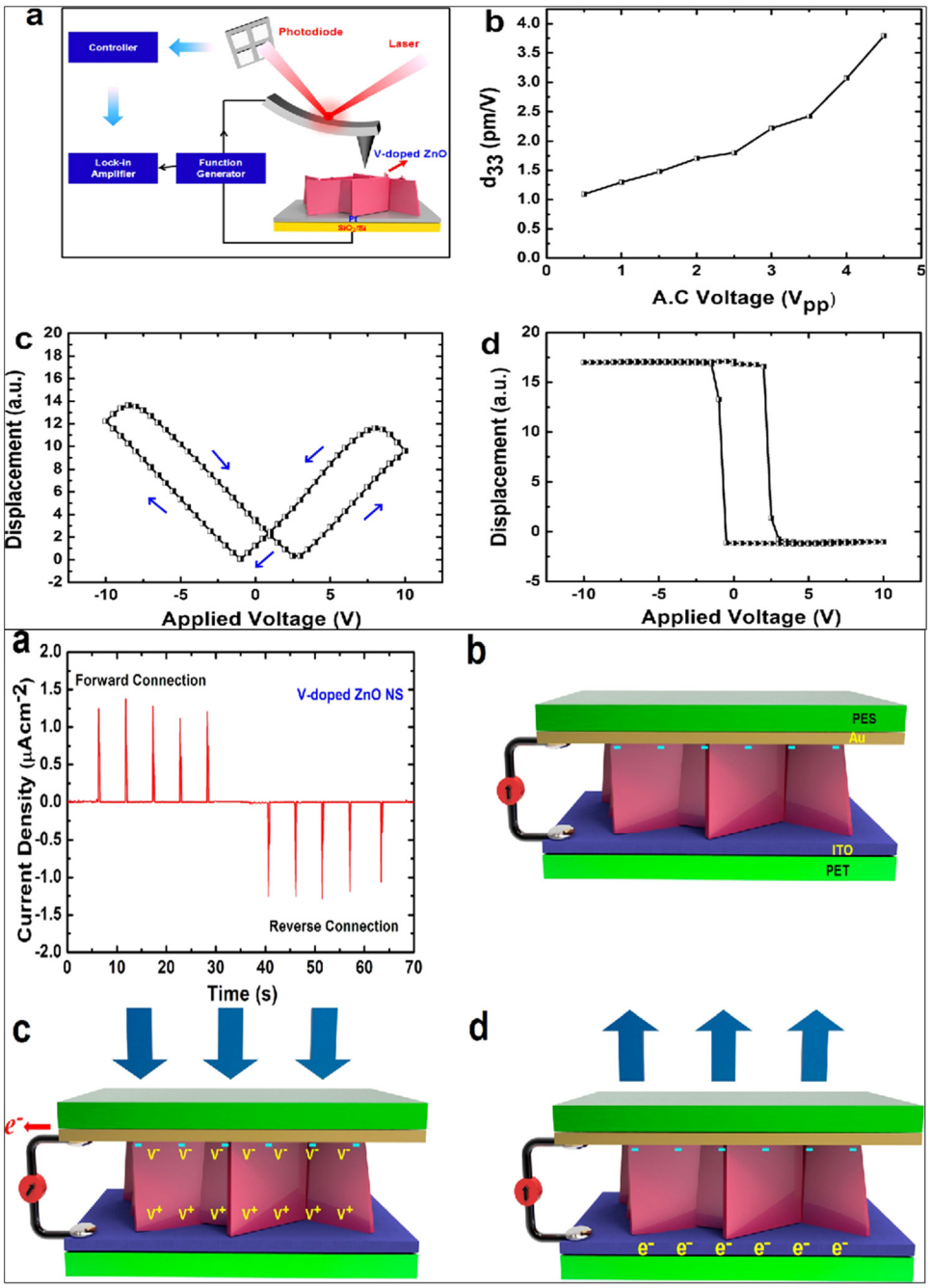

Fig. 21 (a) Experimental diagram of the piezoelectric response (d_{33}) measurement through the PFM setup. (b–d) Butterfly curve and phase-voltage hysteresis curve. (e) The current density obtained from the V-doped ZnO nanosheets showing DC-type charge generation. Mechanism of charge generation of the V-doped ZnO device. Reprinted with permission from ref. 272. Copyright 2013 American Chemical Society.

The authors suggested that the antioxidant property was stronger in the sample without annealing because the FTIR study revealed that the antioxidant components were adsorbed on the NPs surface in the unannealed sample. Kamaraj *et al.*[255] investigated the antioxidant action of SnO_2 NPs obtained using *Cleistanthus collinus*. The authors noticed that with the increase in concentration and time, the antioxidant activity also was enhance. Similarly, Vidhu *et al.*[247] confirmed that the % of the free radical scavenging action increases with an increase in the concentration of NPs, as represented in Fig. 18(a). Khan *et al.* determined the free radical scavenging property of the un-doped, Co-doped SnO_2 NPs and plant extract, considering butylated hydroxytoluene (BHT) as standard, as shown in Fig. 18(b). The maximum and significant DPPH radical scavenging ability of Co-doped SnO_2 NPs was 40, 59, 78 and 88% at different concentrations of 25, 50, 75 and 100 μg ml^{-1}, respectively.

Nanocomposites of SnO_2 with noble metals such as Ag display good efficacy against free radicals with an IC_{50} value of 0.73 mM taking Quercetin as a standard antioxidant, as elucidated by Sinha *et al.*[256] However, the authors did not report on any insight mechanism to support the results.

4.6 Anticancer activity of SnO_2 nanostructures

As per the literature, SnO_2 nanostructures are well known for their anticancer activity. Khan *et al.*[252] synthesized SnO_2 NPs and Co-doped SnO_2 NPs by green methods, utilizing the *Clerodendrum inerme* extract. The obtained NPs were evaluated for their anticancer propensity against mammary gland breast cancer (MCF-7) cell lines. At different concentrations of 25, 50, 75 and 100 μg ml^{-1}, Co-doped SnO_2 NPs were observed to exhibit considerable mortality rate compared to the un-doped SnO_2 NPs. The IC_{50} value after 48 h of incubation (*vs.* the control) for the Co-doped SnO_2 NPs was 18.15 ± 1.0 μg ml^{-1} compared to 31.56 ± 1.4 μg ml^{-1} and 26.99 ± 1.9 μg ml^{-1} for the plant extract and un-doped SnO_2 NPs, respectively. In another report by Li *et al.*,[257] the authors found that SnO_2 NPs of particle size 27.45 ± 13.4 nm exerted a cytotoxic effect on the human oral cancer cell line, CAL-27. Compared to the control, the SnO_2 NPs (50, 100, 200 μg ml^{-1}) (all $P < 0.05$) exhibited a significant decrease in the proliferation activity of the cancer cells. The cell inhibition was noticed to be higher at 48 h than at 24 h. At the concentration of <50 μg ml^{-1}, no substantial cell proliferation was analysed (all $P > 0.05$). In addition, nanoporous materials are currently attracting attention because the mesoporous nanomaterials can penetrate the irregular vascular structure of tumor tissues, and thus enhance the antitumor effect and reduce the associated side effects. Lv *et al.*[258] synthesized mesoporous folate-functionalized SnO_2 nanofibers and analyzed their effects on tumor cells. The average outer diameter of the obtained nanofibers was estimated to be 200 nm, and the wall thickness was 50 nm. *In vitro* and *in vivo* experiments revealed that the nanofibers could significantly inhibit the growth of SMMC-7721 cells.

Multifunctional ZnO/SiO_2 core/shell nanoparticles for bioimaging and drug delivery application have also been reported by G. D. Venkatasubbu and his team. Due to their biocompatibility and low cost, ZnO nanoparticles have been used for the bioimaging and drug delivery application. ZnO nanoparticles were prepared by the co-precipitation method, and the ZnO/SiO_2 core/shell nanoparticles were developed (Fig. 19a–d). The drug release profile of the curcumin-loaded ZnO/SiO_2 core/shell nanoparticles was reported. It was found that the high surface area and low toxicity make ZnO/SiO_2 an appropriate material for drug delivery applications, where the drug is attached to the surface of the silica shell due to hydrogen bonding and electrostatic interaction, and a sustained drug release of 80% of the drug occurs within 24 h with an obtained variance of $P < 0.001$.[259]

5. Piezoelectric nanogenerator for energy harvesting

5.1 ZnO-based piezoelectric nanogenerator

Piezoelectric nanogenerators have been proven as emerging nanodevices to harvest the mechanical energy from various sources, including air flow, vibration, rain drop, walking, and blood flow.[260–262] Semiconducting piezoelectric ZnO nanostructures exhibit superior properties over other piezoelectric nanomaterials due to the easy fabrication of piezoelectric diodes, piezophotonics, and piezophototronics devices. The 1D piezoelectric ZnO nanostructures have been utilized for flexible

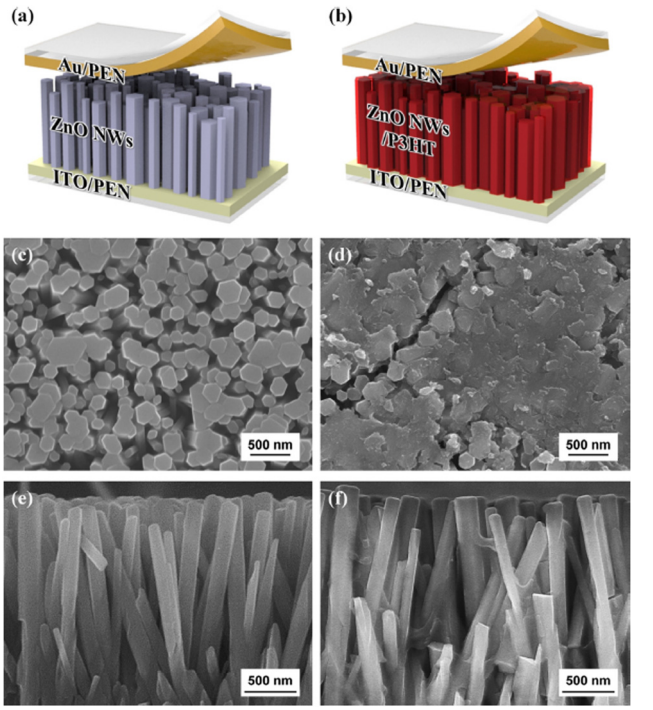

Fig. 22 (a) Schematic image of the pristine ZnO NWs nanogenerator and (b) P3HT-ZnO NWs-nanogenerator. (c) Top view morphology of the pristine ZnO NW and (d) P3HT-coated ZnO NWs. (e and f) Cross-sectional morphology images of the ZnO NWs and P3HT-ZnO NW. Reprinted with permission from ref. 273. Copyright 2014 Elsevier.

piezoelectric nanogenerators, Schottky contact-based nanosensors, and self-powered piezotronics strain sensors.[263–270]

In 2006, vertically aligned zinc oxide nanowire arrays were used as piezoelectric active materials by Z. L. Wang and his team, and they successfully demonstrated the energy-harvesting application using atomic force microscopy. They measured the output voltage by AFM technique using a Pt-coated Si tip with a cone angle of 70° (Fig. 20). They successfully demonstrated the creation of a strain field *via* coupling the semiconducting and piezoelectric properties of zinc oxide NWs. The efficiency of the power generator based on the piezoelectric property of zinc oxide was reported to be in the range of 17–30%.[271]

Gupta *et al.* fabricated vanadium (V) doped ZnO nanosheets (NS) to enhance the piezoelectric properties of pristine ZnO nanostructures.[272] They reported that by vanadium doping, the nanorods-like morphology was transformed into nanosheets. It was reported that with the shielding effect and presence of the OH-ions, the nanorods were converted into nanosheet structures. The V-doped ZnO nanosheets show a d_{33} value of 4 pm V^{-1}, measured through the PFM technique. They reported that the piezoelectricity of the V-doped ZnO nanosheets was greatly improved, which is due to the generation of a large polarization in the V-doped ZnO NS originating from the rotation of the Zn–O bonds and V–O bonds. The high

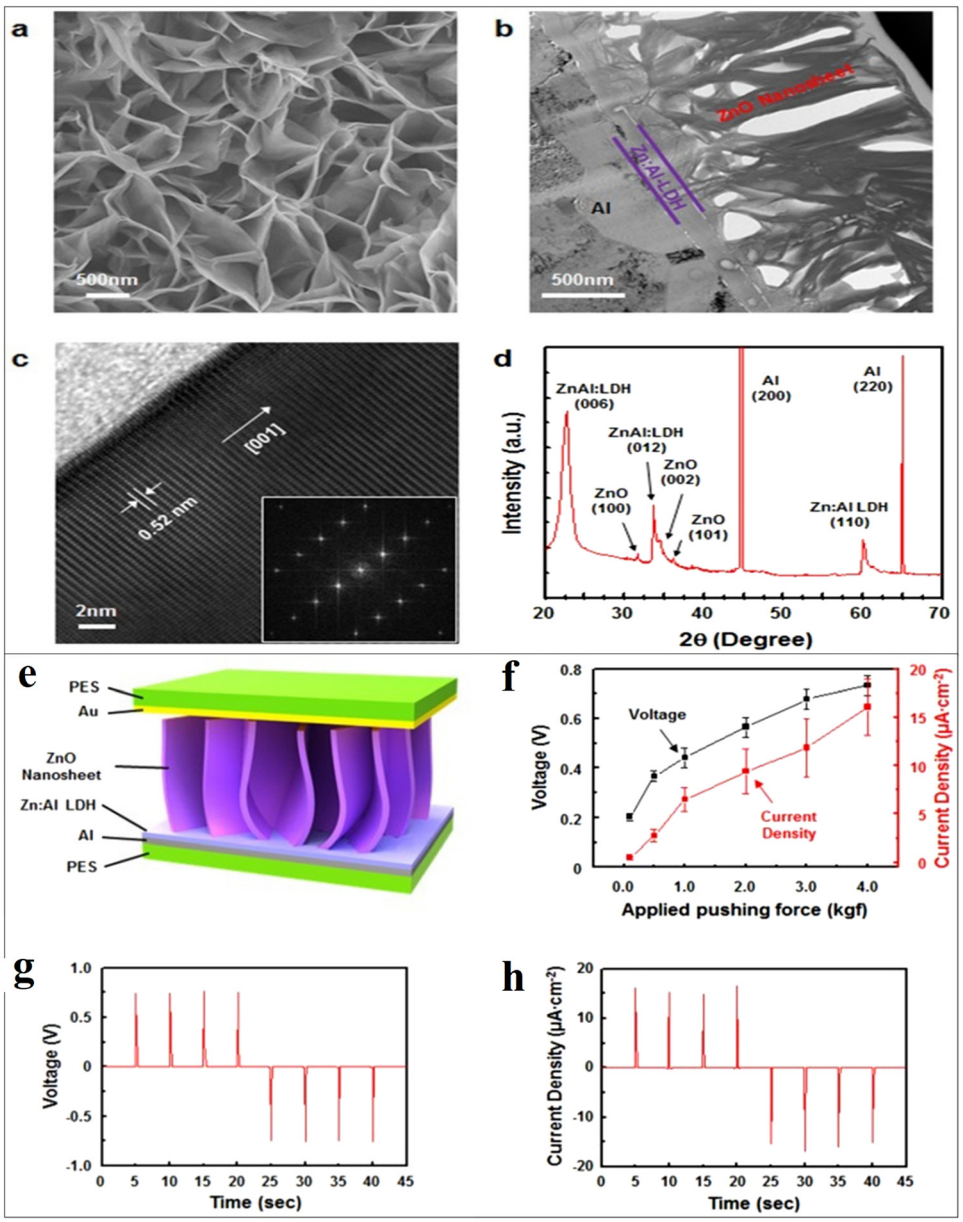

Fig. 23 (a) Morphology of the ZnO nanosheets network structure grown on an Al substrate. (b) TEM (cross-sectional image) of the ZnO nanosheets network. (c) HR TEM image and corresponding FFT pattern (inset). (d) Synchrotron XRD pattern of the ZnO nanosheets (e–g). Schematic image and output voltage from the ZnO nanosheet-based nanogenerator. (h) Measured current density of the ZnO nanosheet-based nanogenerator. Reprinted with permission from ref. 277. Copyright 2013 Springer Nature.

piezoelectric constant is also due to the noncollinear V–O bonds, which has stronger polarity than the Zn–O bonds and can rotate easily under an electric field. A high-performance piezoelectric nanogenerator was fabricated using the flexible ITO-coated PET substrate. The authors reported that the V-doped ZnO nanosheets-based device under a vertical compressive force of 0.5 kgf generates a DC-type current of 1.0 μA cm^{-2}, while the ZnO nanorods generates an AC-type signal of ~10 nA cm^2 under the same condition (Fig. 21). They confirmed that the output performance increased due to the network structure of the ZnO nanosheets.[272] K. Y. Lee *et al.* also developed a piezoelectric nanogenerator based on one-dimensional zinc oxide (ZnO) nanowires (NWs). They improved the output performance of the ZnO NWs-based nanogenerator by controlling the energy band at the depletion width through a p-type semiconductor polymer and native defects. The authors synthesized the vertically aligned flexible ZnO nanowires on the ITO-PEN substrate using the seed-assisted solution technique. A p-type P3HT polymer-coating over the ZnO nanowires was used to increase the performance of the energy-harvesting device. The output performance was increased several times compared to the output voltage of the pristine ZnO NWs-based nanogenerator (Fig. 22). Due to the p-type nature and presence of the holes, drastically decreases

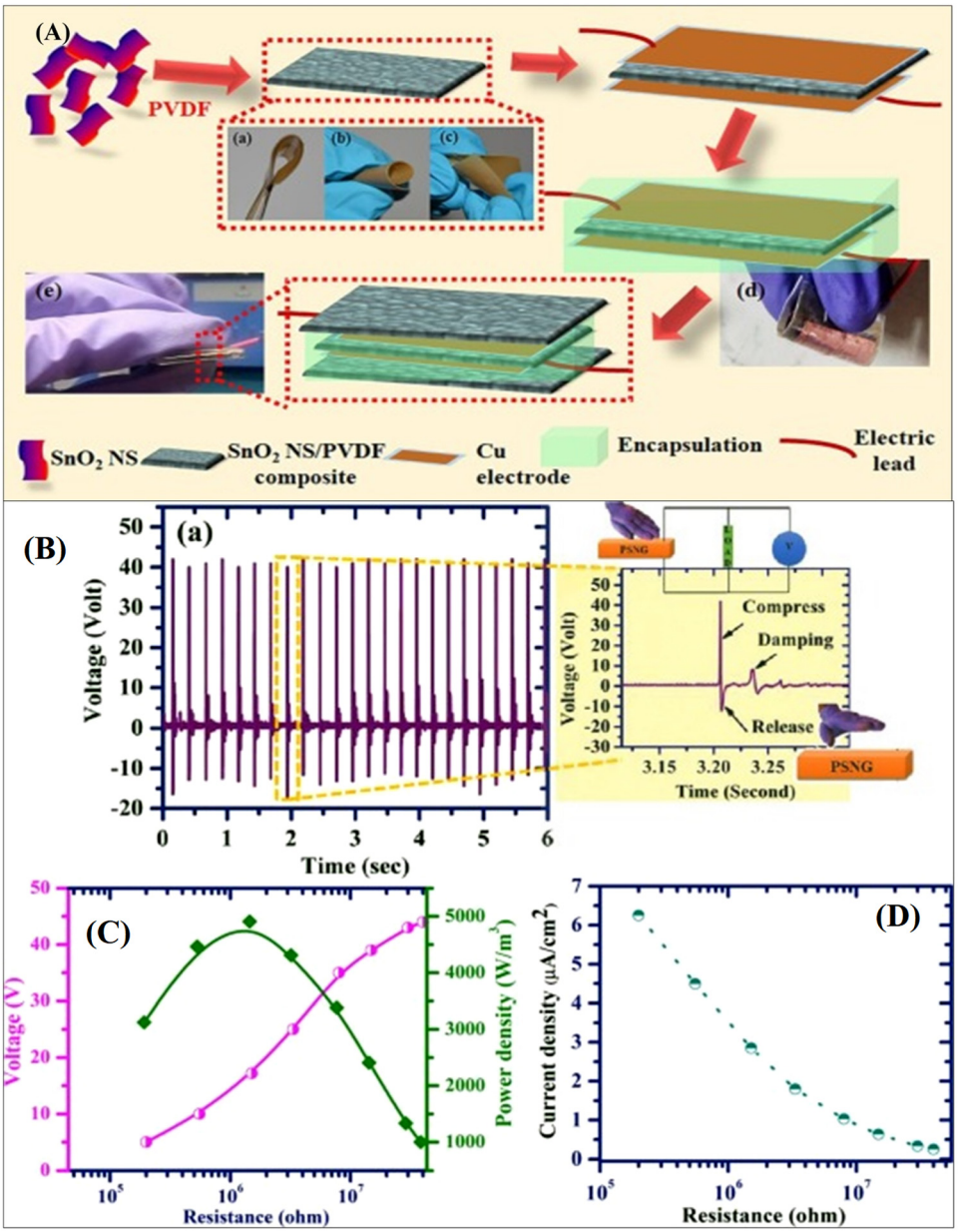

Fig. 24 (A) Schematic image of the fabrication procedure of the SnO_2NS/PVDF-based nanogenerator (a–e). (B) Output voltage produced from the SnO_2NS/PVDF nanogenerator. (C) Variation of the output voltage and (D) power density with load resistance. Reprinted with permission from ref. 282. Copyright 2019 Elsevier.

the piezoelectric screening effect caused by the ZnO free electrons, the resulting output voltage improved.[273]

K.-H. Kim *et al.* reported on the pristine 2D zinc oxide nanosheets and anionic nanoclay layer-based nanogenerator for scavenging mechanical energy. They successfully demonstrated the collective effect of the semiconducting, piezoelectric, buckling property of ZnO NS on the performance of the nanogenerator, and an efficient DC-type output power voltage was obtained. Several electrodes (Au, graphene, indium tin oxide (ITO), and Al) were used to investigate the performance of the ZnO-based nanogenerator. The output performance of the nanosheet nanogenerator was measured using a force simulator. The output voltage and output current density were about 0.44 V and 6.5 μA cm^{-2}, respectively, under 1 kgf. They reported that the output performances of the voltage and current were higher in the case of the Au top electrode, as compared to the graphene, ITO and Al top electrode (Fig. 23). The results also indicated that the nanosheets-like morphology is preferable over the nanorods-like morphology due to the enhanced mechanical properties, especially for nanogenerator applications.[274]

It has been shown that morphological changes greatly affected the output performance of the piezoelectric nanogenerator due to the high surface-to-volume ratio and good mechanical durability. The change in the output performance was due to the change in the piezoelectric polarization and piezoelectric charge coefficient. Gupta *et al.* showed that the V-doping morphology of the ZnO nanorods (1D) converted them into ZnO nanosheets (2D). This was due to the crystallographic growth shielding effect on the c-axis and preferred growth along the a-axis of ZnO, which was caused by the formation of V(OH) ions on the positively charged (0001) Zn-terminated surface, enabling an enhanced DC type current output to be obtained. The occurrence of the DC type electric signal, rather than an AC type electric signal, from the 2D ZnO nanosheets is due to the presence of OH^- ions. Owing to the anisotropic crystal property of the ZnO nanosheets, the effect of the direction of the force, magnitude of the force, and the bending degree on the piezo-potential of the nanogenerator have been reported by Ang Yang and his team. They reported that the 2D structures show high durability due to the interconnected structures. The 2D structures tolerate relatively large

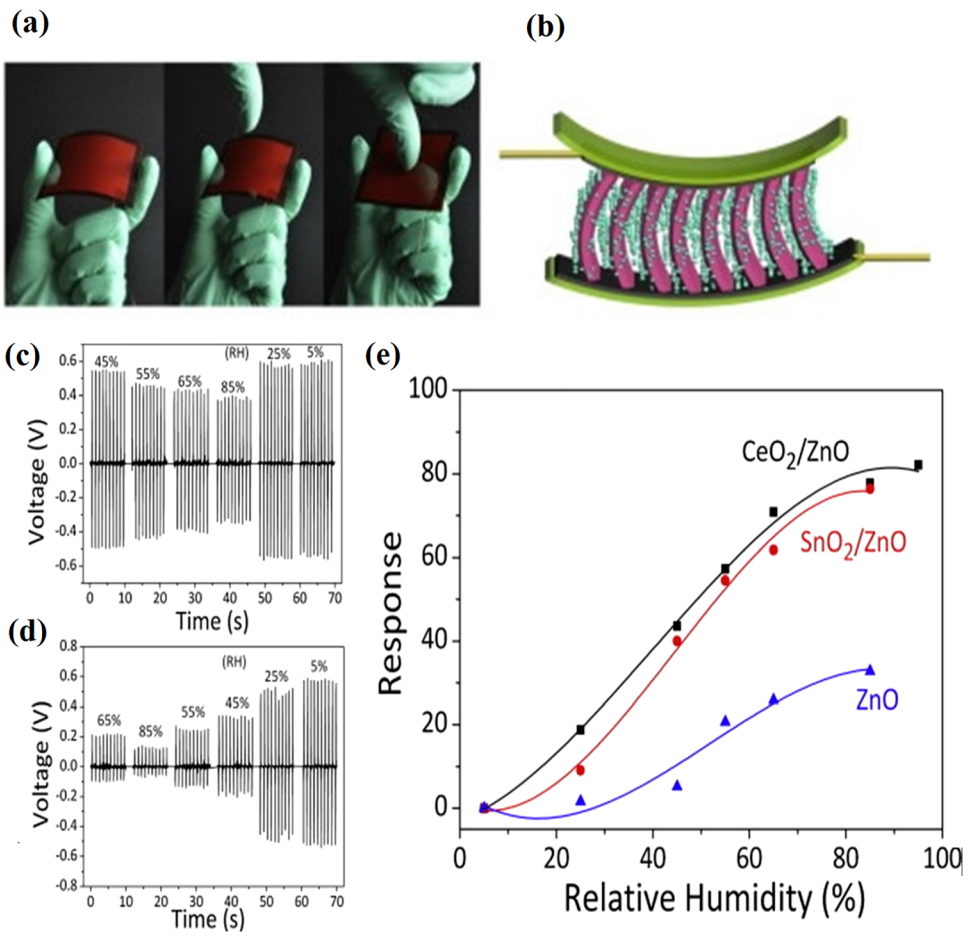

Fig. 25 (a and b) The original picture of the ZnO/SnO_2-based flexible device under compressive deformation through human fingers. (c and d) Piezoelectric output voltage signal measured under different relative humidity conditions. (e) Response of the device under different relative humidity conditions. Reprinted with permission from ref. 284. Copyright 2014 Elsevier.

deformations prior to fractures, demonstrating the high stability of the material.[275–277]

5.2 Tin Oxide (SnO_2):PVDF and SnO_2/ZnO-based piezoelectric nanogenerators

Tin oxide (SnO_2) exhibits a large band gap n-type semiconductor nature, which then makes it suitable for various technological applications in various fields, including infrared detectors, solid state gas sensors, photodetectors optical devices, and heat reflecting mirrors.[278–281] The piezoelectric properties of the pristine SnO_2-based nanostructures are rarely reported. The SnO_2 nanostructures were recently reported as reinforcement materials to fabricate a piezoelectric nanocomposite nanogenerator. The 2D-based SnO_2 nanosheet/PVDF composites-based piezoelectric nanogenerator was fabricated by E. Kar *et al.*[282] The ultrathin 2D SnO_2 nanosheets were grown by hydrothermal method. They fabricated the SnO_2NS/PVDF nanocomposite-based nanogenerator to convert mechanical to electrical energy. The SnO_2 sheet improved the piezoelectric properties of the PVDF, and the output voltage dramatically increased. They fabricated a human body motion-based nanogenerator. The authors demonstrated that the inorganic–organic 2D SnO_2 nanosheet/PVDF composite-based piezoelectric nanogenerators produced a high output voltage of 42 V and current density of 6.25 $\mu A \cdot cm^{-2}$ under gentle human finger tapping (Fig. 24). It was also proposed that the incorporation of homogeneously distributed 2D SnO_2 nanosheets improved the performance of the self-polarized composite due to the high surface area that increased the β phase in PVDF composites. The output power was used to illuminate the 85 light emitting diodes *via* bridge rectifiers. The self-cleaning performance of the SnO_2-PVDF nanogenerator was also demonstrated.[282]

A humidity sensing based on the piezoactive SnO_2/ZnO nanoarray-based nanogenerator with high electrical response and high detecting range was developed by D. Zhu *et al.*[283] The SEM image of the SnO_2/ZnO NW arrays revealed the uniform coating with many SnO_2 nanoparticles on ZnO nanowires. The authors fabricated the piezoelectric humidity sensor device, and their device performances were measured under different humidity conditions. They demonstrated a piezoelectric output voltage of 0.55 at 5% RH, 0.50 at 25% RH, 0.33 at 45% RH, 0.25 at 55% RH, 0.21 at 65% RH, and 0.13 in a relative humidity condition of 85% from the SnO_2/ZnO NW arrays-based nanogenerator (Fig. 25). The piezoelectric voltage decreased with the increase in relative humidity of the atmosphere, and the response of the hybrid SnO_2/ZnO arrays as the piezo/active humidity sensor was high.[283]

The piezoelectric semiconductor coupling properties of the n-type ZnO nanostructures with various morphologies were used to improve the performance of numerous devices. Such dramatic coupling behavior of the semiconducting and piezoelectric properties have recently developed the new concept of piezotronics and piezo-phototronics devices. Owing to this

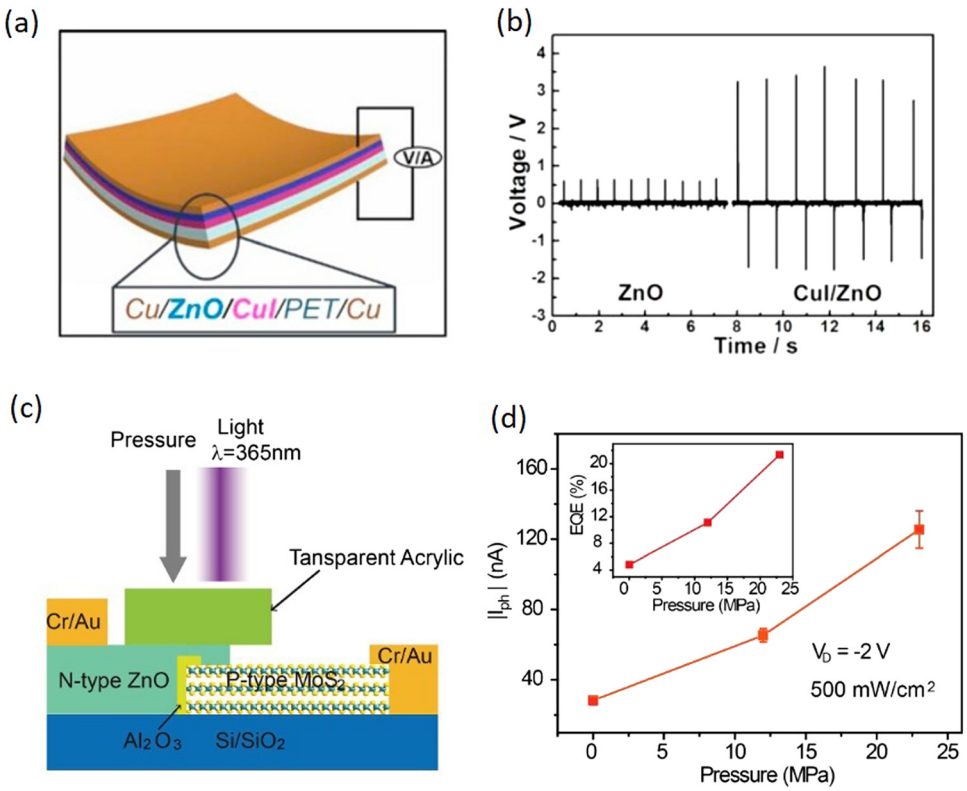

Fig. 26 (a) Schematic presentation of the ZnO/CuI-based piezoelectric photodetector and nanogenerator (b) output voltage of the pristine and ZnO–CuI-based devices. Reprinted with permission from ref. 285. Copyright 2016 Elsevier. (c) Piezotronics device based on ZnO and MoS_2. (d) Piezo-photoresponse from the piezotronics FET device. Reprinted with permission from ref. 288. Copyright 2016 John Wiley and Sons.

coupling behavior, the performance of the ZnO-based photodetector and solar cell have been tuned by the piezoelectric effect caused by mechanical deformation and interface engineering.[284] Recently, J. Zhai and his team used the n-type ZnO thin film and developed a photodetector using the p-type CuI film. They have shown that by using the p-type CuI and engineering the interface between ZnO and CuI, the piezoelectric performance of the ZnO-based nanogenerator improved from 0.8 V to 5.0 V by the formation of a p-CuI/n-ZnO junction (Fig. 26). In addition, it was shown that the piezo-phototronic effect enhanced the photoresponsivity by up to 384%. The high performance is due the reduction of the screening effect due to free electrons in n-type ZnO.[285] Moreover, a piezoelectric nanogenerator based on ZnO nanostructures doped with various halogen elements (fluorine, chlorine, bromine, and iodine) has also been reported by Yang Zhang *et al.*[286]

The performance of the nanogenerator was increased by the lattice strain-induced charge separation under the compressive and tensile state along the ZnO *c*-axis. The piezo-photonics application of the flexible vertically aligned Li-doped ZnO nanowires-based piezotronic transistor array for in-plane strain mapping has also been reported by Z. L. Wang and his team.[287] In addition, the semiconductor nanoarrays were used to established a force mapping method based on a "light nanoantenna" array using the concept of the piezo-phototronic effect. Similarly, a n-type ZnO thin film was used to fabricate the photodetector, along with the p-type MoS_2 nanoflakes by Xiu *et al.* It was reported that the hybrid device showed an excellent rectification ratio and very strong photoresponse. An external quantum efficiency of 52.7% and a response time of 66 ms were obtained under 365 nm optical irradiation. Such improvement in the high photocurrent was obtained through the piezophototronic effect energy band modification under application of the compressive strain (Fig. 26c and d).[288] The piezo-photonics application of the semiconducting nanostructures were also used for the real-time imaging of living cells traction force as performed by Q. Zheng *et al.* This dynamic mapping of living cells provides great insight for detecting the cardiovascular activities of the heart. A light nano-antenna array with the use of the piezo-phototronic effect has been demonstrated.[289]

The morphological evaluation of the ZnO semiconductor has drastically changed the device performances. Zhong Lin Wang and his team investigated the role of the 2D morphology of the semiconductor and piezoelectric ZnO on the output performance of the nanogenerators. It was also demonstrated that the 2D ZnO nanosheets-based nanogenerator showed high current density and output voltage as compared to the 1D ZnO nanorods. Recently, L. Wang *et al.* demonstrated the 2D piezotronics in atomically thin zinc oxide sheets. They fabricated the device based on the solution-grown 2D ZnO nanosheets. The inner crystal out-of-plane potential generated in the atomically thin ZnO surfaces under stress/strain by the piezoelectric polarization simultaneously modulates the metal-ZnO Schottky barrier height and the conductive channel

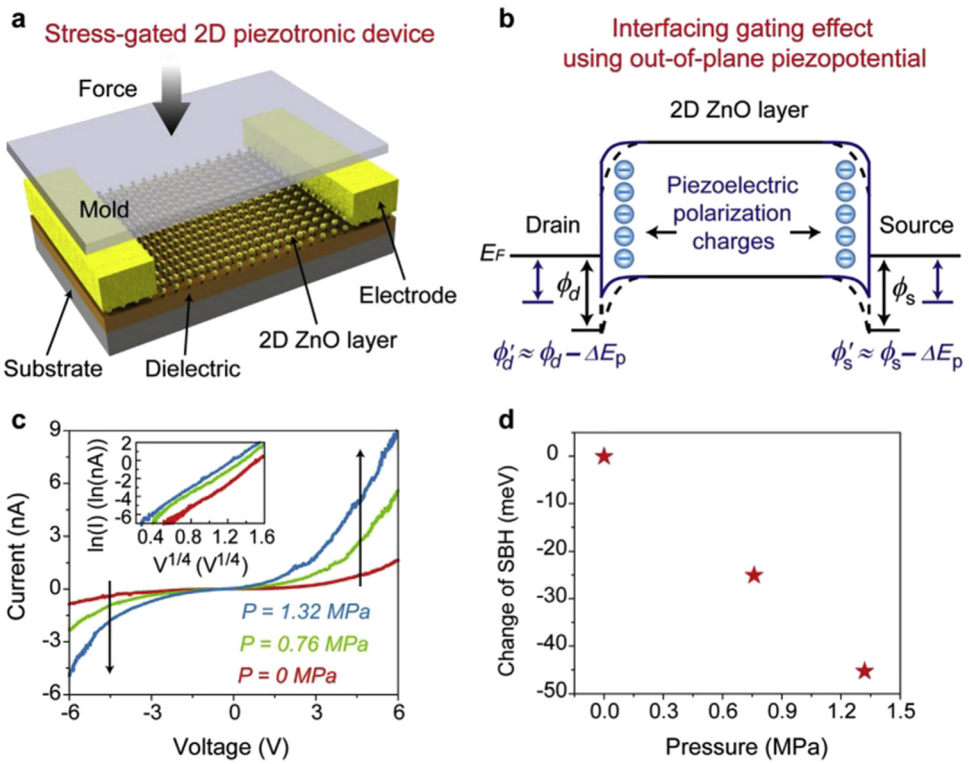

Fig. 27 (a and b) Schematic device diagram of the stress-gated 2D layer-based piezotronics device and band diagram. (c) *IV* characteristic of the 2D ZnO FET piezotronics device under mechanical stress. (d) Response of the SBH with application of the pressure from the device. Reprinted with permission from ref. 129. Copyright 2019 Elsevier.

width of ZnO. Therefore, the electronic transport processes in the two-terminal devices were effectively tuned by an external mechanical force. They also reported the thickness dependence of the 2D piezotronics in interfacing gating and channel width gating. Zhong Lin Wang and his team developed the ultrathin piezotronic transistors with 2-nanometer channel lengths using the ZnO nanostructure. A strain-gated FET piezotronics device was fabricated. The performance of the 2D-based device was measured under application of the pressure, and the IV characteristics were also measured. It was observed that the charge carrier transport characteristics of these devices are effectively gated by the piezoelectric polarization charges created at the Schottky metal-semiconductor interface (Fig. 27 and 28).[129,130]

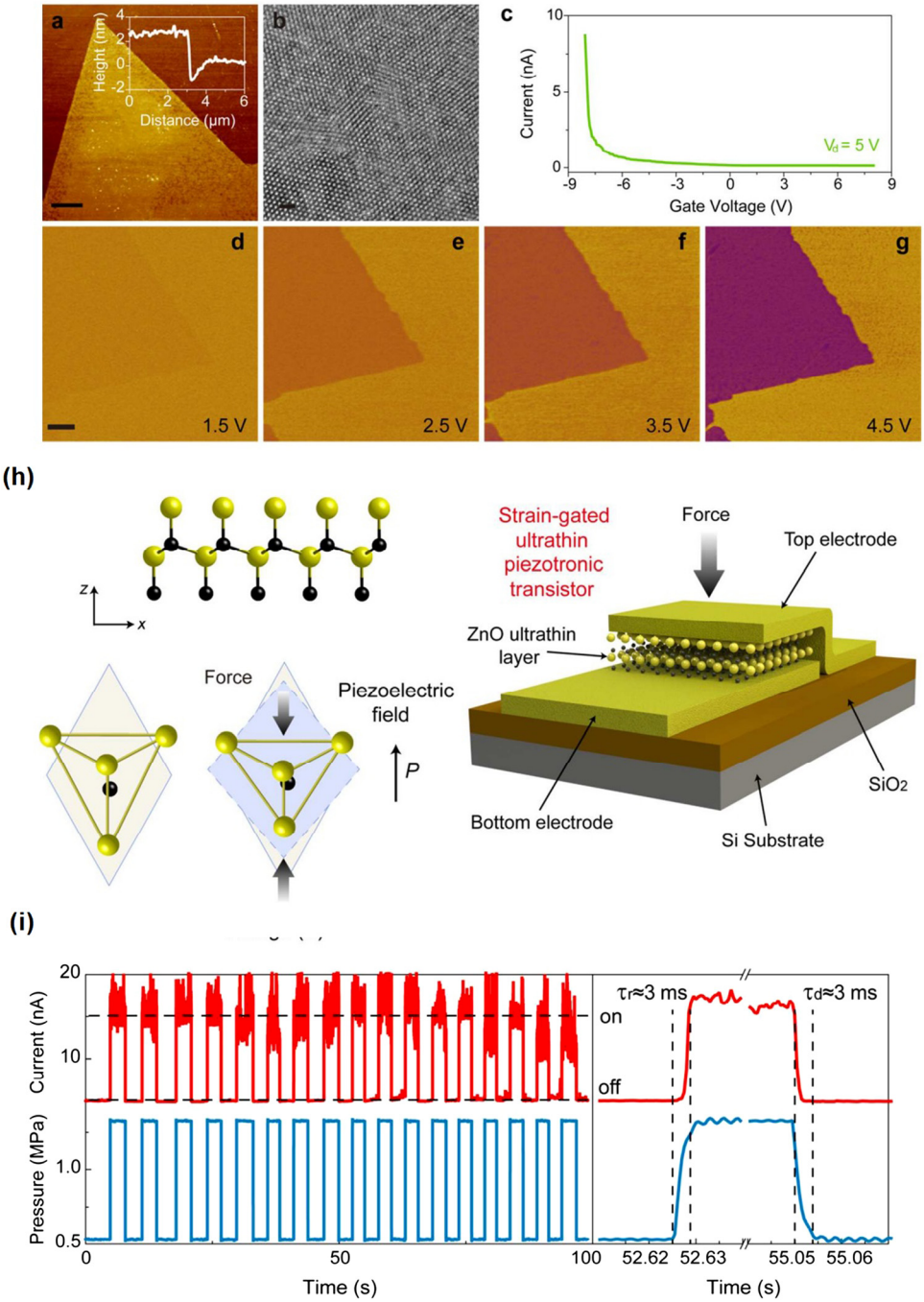

Fig. 28 (a) AFM topography image of the ultrathin film ZnO nanosheets. (b) HRTEM image of the ZnO ultrathin film. (c) Electronic property of the ZnO ultrathin film showing the p-nature of the ZnO ultrathin film. (d–g) Amplitudes *versus* applied voltages (1.5–6.5 V), showing inverse piezoelectricity. (h) Schematic presentation of the ultrathin piezotronic 2D ZnO-based transistor. (i) Real-time measurement of the current through an ultrathin piezotronic transistor. Reprinted with permission from ref. 130. Copyright 2018 American Chemical Society.

Table 1 Comparison of the piezoelectric output performance of ZnO and SnO_2 nanostructures-based nanogenerators

S. no.	Nanostructures	Output voltage	Output current/ current density	Ref.
1	V-ZnO nanosheet	—	1.5 μA cm^{-2}	272
2	Pure ZnO nanosheet	0.44 V	6.5 μA cm^{-2}	274
3	SnO_2/PVDF nanocomposite	42 V	6.25 μA cm^{-2}	282
4	SnO_2/ZnO NW arrays	0.55 V	—	283
5	ZnO nanostrands	150 mV	400 nA	290
6	ZnO nanorods	~3 V	20 nA	291
7	Li-ZnO nanowires	~180 V	~50 μA	292
8	Sound driven ZnO nanowire	50 mV	—	293
9	ZnO nanodiscs	17 V	150 nA	294
10	NiO-ZnO heterostructure	430 mV	40 nA cm^{-2}	295
11	Au-ZnO nanorods	2V	1 μA cm^{-2}	296
12.	ZnO nanosheet	0.924 V	6 μA	297
13	ZnO nanowires film	1.5 V	25 nA	298
14	ZnO nanotubes	35 mV	—	299
15	ZnO-polycarbonate nanocomposites	1.15 V	100 μA	300

The output voltage and current density obtained from various piezoelectric nanogenerators based on different morphologies of the ZnO and SnO_2 nanostructures are summarized in Table 1. The results showed that the change in the morphologies of the piezoelectric nanostructures led to the drastic changes in the output performances of the nanogenerators.

6. Conclusions and future outlook

This current review discussed and analyzed the recent works that addressed the synthesis of the various metal oxide nanostructures and their potential uses as solar cells, humidity sensors, and applications in biomedical and piezoelectric nanogenerators. This review has extensively discussed the effect of the morphologies of the two metal oxides, ZnO and SnO_2 nanostructures, on the growth parameters and their crystal growth habits. The importance of the ZnO nanostructures, such as ZnO and SnO_2 tetrapod-like morphologies, for versatile applications are discussed in detail. The surface modification of ZnO and SnO_2, and the other device enhancement factors (like the particle size, concentration, morphologies, defect and charge transports) in the ZnO and SnO_2 metal oxide nanostructures are summarized. The power conversion efficiencies of the flexible perovskite and dye-sensitized solar cells have a significant impact on the band gap and crystalline defects presented in the metal oxide nanostructures. Various combinations of metal oxide nanostructures with interfacial modifications have been reported to improve the performance and stability of the solar cell. Biological application of the ZnO and SnO_2 nanostructures as antimicrobial agents, anticancer agents and their antilarvicidal activity are presented in the current review, as these materials exhibits unique physicochemical and structural properties, such as shape, zeta potential, crystallinity and porosity. The effective potency of the ZnO nanostructures against various viruses, including SARS-COV-2, has also been discussed. Furthermore, the review article covers the interesting applications of the ZnO nanostructures as flexible piezoelectric nanogenerators and as tiny energy-harvesting devices. The 1D and 2D ZnO nanostructures and their morphological effects on the output performance of the flexible piezoelectric nanogenerator are also addressed. In addition, this review shows that the doping, defects control and surface passivation in the metal oxide nanostructures can tailor the performance of the nanogenerator. Moreover, the application of the metal oxide SnO_2 nanostructures as reinforcement materials with various polymers as a flexible nanogenerator and the effect of SnO_2 on the device performance were discussed. The morphological change in the metal oxide nanomaterials can enhance the efficiency of solar cells, sensor, biological activity and output performance of the piezoelectric nanogenerators. Despite many studies and the progress that has been made so far in terms of the morphological importance of the metal oxide nanostructures, there is still much room for further growth and device performance improvements. The major challenges that need to be controlled are the various types of native defects in the nanostructures to achieve their superior applications in the sensors and solar cells. With a strong interfacial bonding and their ability to bind with the various viruses, antibodies with the nanostructure surfaces are among the critical parameters that need to be enhanced. Moreover, in terms of increasing the performance of the piezoelectric nanostructures-based nanogenerator, especially for the output current density, the interfaces of the top and bottom electrodes with optimized work functions need to be more effective than the present progress. Moreover, the integration of the ZnO and SnO_2 nanostructures with the polymer and their dispersion also need to improve. Overall, the coupling of the piezoelectric nanogenerator along with the solar cell system and biosensors has lead to the creation and design of a new and sustainable efficient hybrid solar-mechanical energy harvester system and the fabrication of self-powered biomedical applications.

Conflicts of interest

The authors declare that there is no conflict of interest.

Acknowledgements

Manoj Kumar Gupta is thankful to CSIR, India for the CSIR-Young Scientist Award (OLP-201) and CSIR Raman Research Fellowship.

References

1 C. Buzea, I. I. Pacheco and K. Robbie, *Biointerphases*, 2007, **2**, MR17–MR71.
2 D. Agarwal, C. O. Aspetti, M. Cargnello, M. Ren, J. Yoo, C. B. Murray and R. Agarwal, *Nano Lett.*, 2017, **17**, 1839–1845.
3 E. Roduner, *Chem. Soc. Rev.*, 2006, **35**, 583–592.
4 R. F. Service, *Science*, 2001, **293**, 782.

5 D. Agarwal, M.-L. Ren, J. S. Berger, J. Yoo, A. Pan and R. Agarwal, *Nano Lett.*, 2019, **19**, 1204–1209.
6 J. N. Tiwari, R. N. Tiwari and K. S. Kim, *Prog. Mater. Sci.*, 2012, **57**, 724–803.
7 A. Glezer, *Russ. Metall. Fuels*, 2011, **4**, 263–269.
8 P. C. Ray, *Chem. Rev.*, 2010, **110**, 5332–5365.
9 K. L. Kelly, E. Coronado, L. L. Zhao and G. C. Schatz, *J. Phys. Chem. B*, 2003, **107**, 668–677.
10 K.-S. Lee and M. A. El-Sayed, *J. Phy. Chem. B*, 2006, **110**, 19220–19225.
11 C. J. Murphy, T. K. Sau, A. M. Gole, C. J. Orendorff, J. Gao, L. Gou, S. E. Hunyadi and T. Li, *J. Phys. Chem. B*, 2005, **109**, 13857–13870.
12 D. Agarwal, J. Yoo, A. Pan and R. Agarwal, *Nano Lett.*, 2019, **19**, 7950–7956.
13 X. Hu, J. Gong, L. Zhang and J. C. Yu, *Adv. Mater.*, 2008, **20**, 4845–4850.
14 L. Qin, J. Xu, X. Dong, Q. Pan, Z. Cheng, Q. Xiang and F. Li, *Nanotechnology*, 2008, **19**, 185705.
15 S. Taguchi, M. Saruyama, T. Teranishi and Y. Kanemitsu, *Phys. Rev. B: Condens. Matter Mater. Phys.*, 2011, **83**, 155324.
16 C. J. Murphy, *Anal. Chem.*, 2002, **74**, 520A–526A.
17 M. Asta, S. M. Kauzlarich, K. Liu, A. Navrotsky and F. E. Osterloh, *Mater. Matters*, 2007, **2**, 3–6.
18 R. Ladj, A. Bitar, M. Eissa, Y. Mugnier, R. Le Dantec, H. Fessi and A. Elaissari, *J. Mater. Chem. B*, 2013, **1**, 1381–1396.
19 A. N. Shipway, E. Katz and I. Willner, *Chem. Phys. Chem.*, 2000, **1**, 18–52.
20 M. Ahamed, M. S. AlSalhi and M. Siddiqui, *Clin. Chim. Acta*, 2010, **411**, 1841–1848.
21 E. Katz and I. Willner, *Angew. Chem., Int. Ed.*, 2004, **43**, 6042–6108.
22 T. M. Tolaymat, A. M. El Badawy, A. Genaidy, K. G. Scheckel, T. P. Luxton and M. Suidan, *Sci. Total Environ.*, 2010, **408**, 999–1006.
23 O. V. Salata, *J. Nanobiotechnol.*, 2004, **2**, 3.
24 L. H. Rashidi, H. Homayoni and W. Chen, *Rev. Nanosci. Nanotechnol*, 2014, **3**, 31–51.
25 X.-M. Qian and S. Nie, *Chem. Soc. Rev.*, 2008, **37**, 912–920.
26 J. L. Elechiguerra, J. Reyes-Gasga and M. J. Yacaman, *J. Mater. Chem.*, 2006, **16**, 3906–3919.
27 J. Li, H. Yu, S. M. Wong, X. Li, G. Zhang, P. G.-Q. Lo and D.-L. Kwong, *Appl. Phys. Lett.*, 2009, **95**, 243113.
28 C. c Delacour, B. Pannetier, J.-C. Villegier and V. Bouchiat, *Nano Lett.*, 2012, **12**, 3501–3506.
29 J. Lee, P. Lee, H. Lee, D. Lee, S. S. Lee and S. H. Ko, *Nanoscale*, 2012, **4**, 6408–6414.
30 Q. Kuang, C. Lao, Z. L. Wang, Z. Xie and L. Zheng, *J. Am. Chem. Soc.*, 2007, **129**, 6070–6071.
31 M. Zhong, D. Xu, X. Yu, K. Huang, X. Liu, Y. Qu, Y. Xu and D. Yang, *Nano Energy*, 2016, **28**, 12–18.
32 D. Akinwande, L. Tao, Q. Yu, X. Lou, P. Peng and D. Kuzum, *IEEE Nanotechnol. Mag.*, 2015, **9**, 6–14.
33 B. K. Teo and X. Sun, *J. Cluster Sci.*, 2006, **17**, 529–540.
34 W. Lu and C. M. Lieber, *Nat. Mater.*, 2007, **6**, 841–850.
35 K. Gregorczyk and M. Knez, *Prog. Mater. Sci.*, 2016, **75**, 1–37.
36 R. S. Devan, R. A. Patil, J. H. Lin and Y. R. Ma, *Adv. Funct. Mater.*, 2012, **22**, 3326–3370.
37 J. Zheng, Q. Jiang and J. Lian, *Appl. Surf. Sci.*, 2011, **257**, 5083–5087.
38 Y. Zhang, L. Wang, X. Liu, Y. Yan, C. Chen and J. Zhu, *J. Phys. Chem. B*, 2005, **109**, 13091–13093.
39 D. Fan, W. Shen, M. Zheng, Y. Zhu and J. Lu, *J. Phys. Chem. C*, 2007, **111**, 9116–9121.
40 W.-J. Lee and G.-H. Lee, *Korean J. Mater. Res.*, 2017, **27**, 530–533.
41 T. Ghoshal, S. Biswas, S. Kar, A. Dev, S. Chakrabarti and S. Chaudhuri, *Nanotechnology*, 2008, **19**, 065606.
42 J. Tawale, K. Dey, R. Pasricha, K. Sood and A. Srivastava, *Thin Solid Films*, 2010, **519**, 1244–1247.
43 A. Khan, S. N. Khan and W. M. Jadwisienczak, *Sci. Adv. Mater.*, 2010, **2**, 572–577.
44 L. Feng, A. Liu, M. Liu, Y. Ma, J. Wei and B. Man, *Mater. Charact.*, 2010, **61**, 128–133.
45 L. Ma, Z. Wei, X. Ye, J. Lin, L. Hu and T. Guo, *Ceram. Int.*, 2017, **43**, 6096–6104.
46 Z. R. Dai, Z. W. Pan and Z. L. Wang, *Adv. Funct. Mater.*, 2003, **13**, 9–24.
47 N. Shaalan, T. Yamazaki and T. Kikuta, *Sens. Actuators, B*, 2011, **153**, 11–16.
48 N. Van Hieu, *Sens. Actuators, B*, 2010, **150**, 112–119.
49 X. Wu, J. Sui, W. Cai and F. Qu, *Mater. Chem. Phys.*, 2008, **112**, 325–328.
50 Y. Lingmin, F. Xinhui, Q. Lijun, M. Lihe and Y. Wen, *Appl. Surf. Sci.*, 2011, **257**, 3140–3144.
51 R. Rahman, S. Karim, D. Kamaruzaman and Z. Zulkifli, *J. Fundam. Appl. Sci.*, 2017, **9**, 909–920.
52 T.-L. Phan, S. Yu, R. Vincent, N. Dan and W. Shi, *J. Lumin.*, 2010, **130**, 1142–1146.
53 M. C. Newton, S. Firth, T. Matsuura and P. A. Warburton, *J. Phys.: Conf. Ser.*, 2006, **26**, 251–255.
54 W. Lee, M.-C. Jeong and J.-M. Myoung, *Acta Mater.*, 2004, **52**, 3949–3957.
55 T. Tillotson, A. Gash, R. Simpson, L. Hrubesh, J. Satcher and J. Poco, *J. Non-Cryst. Solids*, 2001, **285**, 338–345.
56 J. Lee, A. Easteal, U. Pal and D. Bhattacharyya, *Curr. Appl. Phys.*, 2009, **9**, 792–796.
57 S. F. Mousavi, F. Davar and M. Loghman-Estarki, *J. Mater. Sci.: Mater. Electron.*, 2016, **27**, 12985–12995.
58 G. S. Wu, T. Xie, X. Y. Yuan, Y. Li, L. Yang, Y. H. Xiao and L. D. Zhang, *Solid State Commun.*, 2005, **134**, 485–489.
59 J. Joo, S. G. Kwon, J. H. Yu and T. Hyeon, *Adv. Mater.*, 2005, **17**, 1873–1877.
60 J. Li, S. Srinivasan, G. He, J. Kang, S. Wu and F. Ponce, *J. Cryst. Growth*, 2008, **310**, 599–603.
61 A. K. Zak, M. E. Abrishami, W. A. Majid, R. Yousefi and S. Hosseini, *Ceram. Int.*, 2011, **37**, 393–398.
62 M. Farhadi-Khouzani, Z. Fereshteh, M. R. Loghman-Estarki and R. S. Razavi, *J. Sol-Gel Sci. Technol.*, 2012, **64**, 193–199.
63 J. Hasnidawani, H. Azlina, H. Norita, N. Bonnia, S. Ratim and E. Ali, *Procedia Chem.*, 2016, **19**, 211–216.

64 S. Bagherian and A. K. Zak, *Mater. Sci. Semicond. Process.*, 2016, **56**, 52–58.
65 I. H. Kadhim and H. A. Hassan, *J. Electr. Mater.*, 2017, **46**, 1419–1426.
66 A. D. Bhagwat, S. S. Sawant, B. G. Ankamwar and C. M. Mahajan, *J. Nano- Electron. Phys.*, 2015, **7**, 04037.
67 Q. Dong, H. Su, D. Zhang and F. Zhang, *Nanotechnology*, 2006, **17**, 3968.
68 S. Gnanam and V. Rajendran, *Dig. J. Nanomater. Bios.*, 2010, **5**, 699–704.
69 A. Beniwal, V. Srivastava and S. Sharma, *Mater. Res. Express*, 2019, **6**, 046421.
70 V. Kumar, P. Rajaram and Y. Goswami, *Optik*, 2016, **127**, 2490–2494.
71 M. Masjedi-Arani and M. Salavati-Niasari, *J. Mol. Liq.*, 2017, **248**, 197–204.
72 S. Sōmiya and R. Roy, *Bull. Mater. Sci.*, 2000, **23**, 453–460.
73 G. W. Morey, *J. Am. Ceram. Soc.*, 1953, **36**, 279–285.
74 S. B. Kondawar, S. A. Acharya and S. R. Dhakate, *Adv. Mater. Lett.*, 2011, **2**, 362–367.
75 B. Cheng and E. T. Samulski, *Chem. Commun.*, 2004, 986–987.
76 E. Kowsari and M. R. Ghezelbash, *Mater. Lett.*, 2012, **68**, 17–20.
77 C. Cheng, B. Liu, H. Yang, W. Zhou, L. Sun, R. Chen, S. F. Yu, J. Zhang, H. Gong, H. Sun and H. J. Fan, *ACS Nano*, 2009, **3**, 3069–3076.
78 K. C. Patil, S. T. Aruna and T. Mimani, *Curr. Opin. Solid State Mater. Sci.*, 2002, **6**, 507–512.
79 K. C. Patil, S. T. Aruna and S. Ekambaram, *Curr. Opin. Solid State Mater. Sci.*, 1997, **2**, 158–165.
80 S. T. Aruna and A. S. Mukasyan, *Curr. Opin. Solid State Mater. Sci.*, 2008, **12**, 44–50.
81 Y.-N. Zhao, M.-S. Cao, H.-B. Jin, X.-L. Shi, X. Li and S. Agathopoulos, *J. Nanosci. Nanotechnol.*, 2006, **6**, 2525–2528.
82 J. Quan, H. A. Colorado, P.-C. Yeh and J.-M. Yang, *Ceram. Int.*, 2016, **42**, 13053–13060.
83 F. Gu, S. F. Wang, M. K. Lü, G. J. Zhou, D. Xu and D. R. Yuan, *Langmuir*, 2004, **20**, 3528–3531.
84 L. Chen, W. Song, C. Xie, L. Lin and J. Wang, *Mater. Lett.*, 2007, **61**, 4603–4605.
85 P. G. Krishna, P. P. Ananthaswamy, P. Trivedi, V. Chaturvedi, N. B. Mutta, A. Sannaiah, A. Erra and T. Yadavalli, *Mater. Sci. Eng., C*, 2017, **75**, 1026–1033.
86 H. H. Nersisyan, J. H. Lee, J.-R. Ding, K.-S. Kim, K. V. Manukyan and A. S. Mukasyan, *Prog. Energy Combust. Sci.*, 2017, **63**, 79–118.
87 B. Babu, A. Kadam, R. Ravikumar and C. Byon, *J. Alloys Compd.*, 2017, **703**, 330–336.
88 Z. Chen, Y. Zhu, Q. Duan, A. Chen and Z. Tang, *J. Am. Ceram. Soc.*, 2019, **102**, 42–47.
89 Z. L. Wang, *J. Phys.: Condens. Matter*, 2004, **16**, R829.
90 W. L. Hughes and Z. L. Wang, *Appl. Phys. Lett.*, 2003, **82**, 2886–2888.
91 S. Minne, S. Manalis and C. Quate, *Appl. Phys. Lett.*, 1995, **67**, 3918–3920.
92 T. Parker, N. Condon, R. Lindsay, F. Leibsle and G. Thornton, *Surf. Sci.*, 1998, **415**, L1046–L1050.
93 O. Dulub, L. A. Boatner and U. Diebold, *Surf. Sci.*, 2002, **519**, 201–217.
94 B. Meyer and D. Marx, *Phys. Rev. B: Condens. Matter Mater. Phys.*, 2003, **67**(2003), 035403.
95 X. Jin, M. Götz, S. Wille, Y. K. Mishra, R. Adelung and C. Zollfrank, *Adv. Mater.*, 2013, **25**, 1342–1347.
96 M. C. Newton and P. A. Warburton, ZnO tetrapod nanocrystals, *Mater. Today*, 2007, **10**, 50–54.
97 D. J. Milliron, S. M. Hughes, Y. Cui, L. Manna, J. Li, L.-W. Wang and A. P. Alivisatos, *Nature*, 2004, **430**, 190–195.
98 J. Gong, S. Yang, H. Huang, J. Duan, H. Liu, X. Zhao, R. Zhang and Y. Du, *Small*, 2006, **2**, 732–735.
99 F. Wang, Z. Ye, D. Ma, L. Zhu and F. Zhuge, *Mater. Lett.*, 2005, **59**, 560–563.
100 Z. Chen, Z. Shan, M. Cao, L. Lu and S. X. Mao, *Nanotechnology*, 2004, **15**, 365.
101 C.-Y. Yeh, Z. Lu, S. Froyen and A. Zunger, *Phys. Rev. B: Condens. Matter Mater. Phys.*, 1992, **46**, 10086.
102 A. Ashrafi and C. Jagadish, *J. Appl. Phys.*, 2007, **102**, 071101.
103 L. Manna, D. J. Milliron, A. Meisel, E. C. Scher and A. P. Alivisatos, *Nat. Mater.*, 2003, **2**, 382–385.
104 H. Yan, R. He, J. Pham and P. Yang, *Adv. Mater.*, 2003, **15**, 402–405.
105 S. Avilov, A. Tuchin, A. Shebanov and E. Domashevskaya, *Crystallogr. Rep.*, 2019, **64**, 212–215.
106 M. C. Newton, S. Firth and P. A. Warburton, *Appl. Phys. Lett.*, 2006, **89**, 072104.
107 Y. K. Mishra, G. Modi, V. Cretu, V. Postica, O. Lupan, T. Reimer, I. Paulowicz, V. Hrkac, W. Benecke, L. Kienle and R. Aelung, *ACS Appl. Mater. Interfaces*, 2015, **7**, 14303–14316.
108 O. Lupan, L. Chow and G. Chai, *Sens. Actuators, B*, 2009, **141**, 511–517.
109 S. Rackauskas, K. Mustonen, T. Järvinen, M. Mattila, O. Klimova, H. Jiang, O. Tolochko, H. Lipsanen, E. Kauppinen and A. G. Nasibulin, *Nanotechnology*, 2012, **23**, 095502.
110 L. Yan, A. Uddin and H. Wang, *Nanomater. Nanotechnol.*, 2015, **5**, 19.
111 S. Rackauskas, O. Klimova, H. Jiang, A. Nikitenko, K. A. Chernenko and S. D. Shandakov, *et al.*, *J. Phys. Chem. C*, 2015, **119**, 16366–16373.
112 Y. K. Mishra, S. Kaps, A. Schuchardt, I. Paulowicz, X. Jin, D. Gedamu, S. Wille, O. Lupan and R. Adelung, *KONA Powder Part. J.*, 2014, **31**, 92–110.
113 Q. Luo, Y. Qiu, P. Xu, D. Zhu, Z. Cheng and H. Fan, *Mater. Lett.*, 2016, **182**, 138–142.
114 W. Yu, X. Li and X. Gao, *Cryst. Growth Des.*, 2005, **5**, 151–155.
115 Y. Ding, Z. L. Wang, T. Sun and J. Qiu, *Appl. Phys. Lett.*, 2007, **90**, 153510.
116 J. Tawale, A. Kumar, A. Mohan and A. Srivastava, *Opt. Mater.*, 2013, **35**, 1335–1341.
117 G. Modi, *Adv. Nat. Sci.: Nanosci. Nanotechnol.*, 2015, **6**, 033002.

118 N. Kopidakis, W. J. Mitchell, J. Van De Lagemaat, D. S. Ginley, G. Rumbles and S. E. Shaheen, *Appl. Phys. Lett.*, 2006, **89**, 103524.
119 D. Calestani, M. Zha, R. Mosca, A. Zappettini, M. Carotta, V. Di Natale and L. Zanotti, *Sens. Actuators, B*, 2010, **144**, 472–478.
120 A. Wei, L. Pan and W. Huang, *Mater. Sci. Eng. B*, 2011, **176**, 1409–1421.
121 Y. Qiu and S. Yang, *Adv. Funct. Mater.*, 2007, **17**, 1345–1352.
122 M. Thepnurat, T. Chairuangsri, N. Hongsith, P. Ruankham and S. Choopun, *ACS Appl. Mater. Interfaces*, 2015, **7**, 24177–24184.
123 K. Sun, J. Qi, Q. Zhang, Y. Yang and Y. Zhang, *Nanoscale*, 2011, **3**, 2166–2168.
124 S. A. Mahmoud and O. A. Fouad, *Sol. Energy Mater. Sol. Cells*, 2015, **136**, 38–43.
125 W. Chen, Y. Qiu and S. Yang, *Phys. Chem. Chem. Phys.*, 2012, **14**, 10872–10881.
126 J. M. Szarko, J. K. Song, C. W. Blackledge, I. Swart, S. R. Leone, S. Li and Y. Zhao, *Chem. Phys. Lett.*, 2005, **404**, 171–176.
127 L. Wei, X. Zhang, B. Wang, C. Lou, Z. Zhu, Z. Zhao, L. Chi and H. Kai, *IEEE Electron Device Lett.*, 2008, **29**, 452–455.
128 D. J. Clark, L. Yuan, C. O. Otieno, G. Zhou and J. I. Jang, *Solid State Commun.*, 2014, **181**, 9–14.
129 L. Wang, S. Liu, Z. Zhang, X. Feng, L. Zhu, H. Guo, W. Ding, L. Chen, Y. Qin and Z. L. Wang, *Nano Energy*, 2019, **60**, 724–733.
130 L. Wang, S. Liu, G. Gao, Y. Pang, X. Yin, X. Feng, L. Zhu, Y. Bai, L. Chen, T. Xiao, X. Wang, Y. Qin and Z. L. Wang, *ACS Nano*, 2018, **12**, 4903–4908.
131 Y. Liu, C. Zheng, W. Wang, C. Yin and G. Wang, *Adv. Mater.*, 2001, **13**, 1883–1887.
132 V. Ivashchenko, B. Rud, A. Gonchar, L. Ivashchenko and O. Butenko, *Powder Metall. Met. Ceram.*, 2012, **51**, 353–362.
133 L. Jiang, G. Sun, Z. Zhou, S. Sun, Q. Wang, S. Yan, H. Li, J. Tian, J. Guo, B. Zhou and Q. Xin, *J. Phys. Chem. B*, 2005, **109**, 8774–8778.
134 S. Pianaro, P. R. Bueno, E. Longo and J. A. Varela, *J. Mater. Sci. Lett.*, 1995, **14**, 692–694.
135 Y. Chen, Q. Li, Y. Liang, T. Wang, Q. Zhao and D. Yu, *App. Phys. Lett.*, 2004, **85**, 5682–5684.
136 Z. Liu, D. Zhang, S. Han, C. Li, T. Tang, W. Jin, X. Liu, B. Lei and C. Zhou, *Adv. Mater.*, 2003, **15**, 1754–1757.
137 Y. Wang, X. Jiang and Y. Xia, *J. Am. Chem. Soc.*, 2003, **125**, 16176–16177.
138 Y. Liu, Y. Jiao, Z. Zhang, F. Qu, A. Umar and X. Wu, *ACS Appl. Mater. Interfaces*, 2014, **6**, 2174–2184.
139 K. Suematsu, Y. Shin, Z. Hua, K. Yoshida, M. Yuasa, T. Kida and K. Shimanoe, *ACS Appl. Mater. Interfaces*, 2014, **6**, 5319–5326.
140 S. Gubbala, V. Chakrapani, V. Kumar and M. K. Sunkara, *Adv. Funct. Mater.*, 2008, **18**, 2411–2418.
141 H. J. Snaith and C. Ducati, *Nano Lett.*, 2010, **10**, 1259–1265.
142 J. S. Chen and X. W. D. Lou, *Small*, 2013, **9**, 1877–1893.
143 X. Zhou, L. J. Wan and Y. G. Guo, *Adv. Mater.*, 2013, **25**, 2152–2157.
144 H. G. Yang and H. C. Zeng, *Angew. Chem.*, 2004, **116**, 6056–6059.
145 J. Hu, X. Ma, N. Shang, Z. Xie, N. Wong, C. S. Lee and S. T. Lee, *J. Phys. Chem. B*, 2002, **106**, 3823–3826.
146 Y. Wang, J. Y. Lee and H. C. Zeng, *Chem. Mater.*, 2005, **17**, 3899–3903.
147 Z. Wang, D. Luan, F. Y. C. Boey and X. W. Lou, *J. Am. Chem. Soc.*, 2011, **133**, 4738–4741.
148 M. S. Park, Y. M. Kang, G. X. Wang, S. X. Dou and H. K. Liu, *Adv. Funct. Mater.*, 2008, **18**, 455–461.
149 Y. Liu and M. Liu, *Adv. Funct. Mater.*, 2005, **15**, 57–62.
150 S. Luo, J. Fan, W. Liu, M. Zhang, Z. Song, C. Lin, X. Wu and P. K. Chu, *Nanotechnology*, 2006, **17**, 1695.
151 H. G. Yang and H. C. Zeng, *Angew. Chem., Int. Ed.*, 2004, **43**, 5930–5933.
152 J. S. Tawale, G. Gupta, A. Mohan, A. Kumar and A. K. Srivastava, *Sens. Actuators, B*, 2014, **201**, 369–377.
153 F. Gu, S. F. Wang, M. K. Lü, G. J. Zhou, D. Xu and D. R. Yuan, *J. Phys. Chem. B*, 2004, **108**, 8119–8123.
154 F. Gu, S. Wang, H. Cao and C. Li, *Nanotechnology*, 2008, **19**, 095708.
155 K. G. Dhinakar, T. Selvalakshmi, S. M. Sundar and A. C. Bose, *J. Mater. Sci.: Mater. Electron.*, 2016, **27**, 5818–5824.
156 E. Albanese, C. Di Valentin, G. Pacchioni, F. Sauvage, S. Livraghi and E. Giamello, *J. Phys. Chem. C*, 2015, **119**, 26895–26903.
157 H. Wang and A. L. Rogach, *Chem. Mater.*, 2013, **26**, 123–133.
158 N. Salah, S. Habib, A. Azam, M. S. Ansari and W. M. Al-Shawafi, *Nanomater. Nanotechnol.*, 2016, **6**, 17.
159 M. Parthibavarman, V. Hariharan and C. Sekar, *Mater. Sci. Eng., C*, 2011, **31**, 840–844.
160 M. Batzill, *Sensors*, 2006, **6**, 1345–1366.
161 A. Tricoli, *Biosensors*, 2012, **2**, 221–233.
162 L.-Y. Jiang, X.-L. Wu, Y.-G. Guo and L.-J. Wan, *J. Phys. Chem. C*, 2009, **113**, 14213–14219.
163 H. Wang, K. Dou, W. Y. Teoh, Y. Zhan, T. F. Hung, F. Zhang, J. Xu, R. Q. Zhang and A. L. Rogach, *Adv. Funct. Mater.*, 2013, **23**, 4847–4853.
164 N. Van Hieu, *Sens. Actuators, B*, 2010, **150**, 112–119.
165 E. Lackner, J. Krainer, R. Wimmer-Teubenbacher, F. Sosada, M. Deluca, C. Gspan, K. Rohracher, E. Wachmann and A. Kock, *Mater. Today: Proc.*, 2017, **4**, 7128–7131.
166 Y. Xu, W. Zheng, X. Liu, L. Zhang, L. Zheng, C. Yang, N. Pinna and J. Zhang, *Mater. Horiz.*, 2020, **7**, 1519–1527.
167 E. Lackner, J. Krainer, R. Wimmer-Teubenbacher, F. Sosada, C. Gspan, K. Rohracher, E. Wachmann and A. Kock, *Procedia Eng.*, 2016, **168**, 297–300.
168 G. Mutinati, E. Brunet, S. Steinhauer, A. Köck, J. Teva, J. Kraft, J. Siegert, F. Schrank and E. Bertagnolli, *Procedia Eng.*, 2012, **47**, 490–493.
169 M. Grätzel, *Nature*, 2001, **414**, 338–344.
170 Q. Zhao, T. Xie, L. Peng, Y. Lin, P. Wang, L. Peng and D. Wang, *J. Phys. Chem. C*, 2007, **111**, 17136–17145.

171 Z. Chen, Y. Tang, C. Liu, Y. Leung, G. Yuan, L. Chen, Y. Wang, I. Bello, J. Zapien, W. Zhang, C. Lee and S. Lee, *J. Phys. Chem. C*, 2009, **113**, 13433–13437.
172 S. Yun, J. Lee, J. Chung and S. Lim, *J. Phys. Chem. Solids*, 2010, **71**, 1724–1731.
173 J. Han, F. Fan, C. Xu, S. Lin, M. Wei, X. Duan and Z. L. Wang, *Nanotechnology*, 2010, **21**, 405203.
174 A. B. Martinson, J. W. Elam, J. T. Hupp and M. J. Pellin, *Nano Lett.*, 2007, **7**, 2183–2187.
175 K. Keis, J. Lindgren, S.-E. Lindquist and A. Hagfeldt, *Langmuir*, 2000, **16**, 4688–4694.
176 Y.-K. Syu, Y. Tingare, C.-Y. Yeh, J.-S. Yang and J.-J. Wu, *RSC Adv.*, 2016, **6**, 59273–59279.
177 C.-P. Lee, C.-T. Li, M.-S. Fan, S.-R. Li, Y.-J. Huang, L.-Y. Chang, C.-M. Tseng, S.-S. Sun, J.-J. Lin and K.-C. Ho, *Electrochim. Acta*, 2016, **210**, 483–491.
178 D. Barpuzary, A. S. Patra, J. V. Vaghasiya, B. G. Solanki, S. S. Soni and M. Qureshi, *ACS Appl. Mater. Interfaces*, 2014, **6**, 12629–12639.
179 J. X. Zhao, Y. Z. Zheng, X. H. Lu, J. F. Chen, X. Tao and W. Zhou, *ChemPhysChem*, 2013, **14**, 1977–1984.
180 N. Eswaramoorthy and R. Kamatchi, *J. Mater. Sci.: Mater. Electron.*, 2021, **32**, 24138–24151.
181 T. Pauportè, *The Future of Semiconductor Oxides in Next-Generation Solar Cells*, Elsevier, 2018, pp. 3–43.
182 L. Zuo, Z. Gu, T. Ye, W. Fu, G. Wu, H. Li and H. Chen, *J. Am. Chem. Soc.*, 2015, **137**, 2674–2679.
183 D. Liu and T. L. Kelly, *Nat. Photonics*, 2014, **8**, 133–138.
184 J. Dong, J. Shi, D. Li, Y. Luo and Q. Meng, *Appl. Phys. Lett.*, 2015, **107**, 073507.
185 K. Mahmood and S. B. Park, *Electron. Mater. Lett.*, 2013, **9**, 161–170.
186 A. Wibowo, M. A. Marsudi, M. I. Amal, M. B. Ananda, R. Stephanie, H. Ardy and L. J. Diguna, *RSC Adv.*, 2020, **10**, 42838.
187 Y.-Z. Zheng, E.-F. Zhao, F.-L. Meng, X.-S. Lai, X.-M. Dong, J.-J. Wu and X. Tao, *J. Mater. Chem. A*, 2017, **5**, 12416–12425.
188 X. Dong, H. Hu, B. Lin, J. Ding and N. Yuan, *Chem. Commun.*, 2014, **50**, 14405–14408.
189 Y. Chen, Y. Hu, Q. Meng, H. Yan, W. Shuai and Z. Zhang, *J. Mater. Sci.: Mater. Electron.*, 2019, **30**, 4726–4736.
190 H. Wang, T. Kubo, J. Nakazaki and H. Segawa, *ACS Energy Lett.*, 2017, **2**, 2110–2117.
191 T. Kawawaki, H. Wang, T. Kubo, K. Saito, J. Nakazaki, H. Segawa and T. Tatsuma, *ACS Nano*, 2015, **9**, 4165–4172.
192 F. Yang, Y. Xu, M. Gu, S. Zhou, Y. Wang, K. Lu, Z. Liu, X. Ling, Z. Zhu and J. Chen, *J. Mater. Chem. A*, 2018, **6**, 17688–17697.
193 J. Yang, J. Lee, J. Lee and W. Yi, *J. Power Sources*, 2019, **421**, 124–131.
194 L. Wang, D.-B. Li, K. Li, C. Chen, H.-X. Deng, L. Gao, Y. Zhao, F. Jiang, L. Li and F. Huang, *Nat. Energy*, 2017, **2**, 1–9.
195 X. Wen, A. Nowak-Król, O. Nagler, F. Kraus, N. Zhu, N. Zheng, M. Müller, D. Schmidt, Z. Xie and F. Würthner, *Angew. Chem.*, 2019, **131**, 13185–13189.
196 F.-I. Lai, J.-F. Yang, W.-X. Liao and S.-Y. Kuo, *Sci. Rep.*, 2017, **7**, 14927.
197 X. Pu, J. Liu, J. Liang, Y. Xia, W. Feng, Y. Wang and X. Yu, *RSC Adv.*, 2014, **4**, 23149–23154.
198 W. Ke, G. Fang, Q. Liu, L. Xiong, P. Qin, H. Tao, J. Wang, H. Lei, B. Li and J. Wan, *J. Am. Chem. Soc.*, 2015, **137**, 6730–6733.
199 I. J. Park, S. Park, D. H. Kim, H. Jeong and S. Lee, *Mater. Lett.*, 2017, **202**, 48–51.
200 S. Gubbala, V. Chakrapani, V. Kumar and M. K. Sunkara, *Adv. Funct. Mater.*, 2008, **18**, 2411–2418.
201 X. Hou, Y. Hu, H. Jiang, J. Huo, Y. Li and C. Li, *J. Mater. Chem. A*, 2013, **1**, 13814–13820.
202 G. S. Han, H. S. Chung, D. H. Kim, B. J. Kim, J.-W. Lee, N.-G. Park, I. S. Cho, J.-K. Lee, S. Lee and H. S. Jung, *Nanoscale*, 2015, **7**, 15284–15290.
203 K. Mahmood, B. S. Swain and A. Amassian, *Adv. Energy Mater.*, 2015, **5**, 1500568.
204 P. Chen, X. Yin, M. Que, Y. Yang and W. Que, *RSC Adv.*, 2016, **6**, 57996–58002.
205 Y. Lv, P. Wang, B. Cai, Q. Ma, X. Zheng, Y. Wu, Q. Jiang, J. Liu and W. H. Zhang, *Sol. RRL*, 2018, **2**, 1800133.
206 C. Gao, S. Yuan, B. Cao and J. Yu, *Chem. Eng. J.*, 2017, **325**, 378–385.
207 Q. Liu, M. C. Qin, W. J. Ke, X. L. Zheng, Z. Chen, P. L. Qin, L. B. Xiong, H. W. Lei, J. W. Wan and J. Wen, *Adv. Funct. Mater.*, 2016, **26**, 6069–6075.
208 G. Yang, H. W. Lei, H. Tao, X. L. Zheng, J. J. Ma, Q. Liu, W. J. Ke, Z. L. Chen, L. B. Xiong, P. L. Qin, Z. Chen, M. C. Qin, X. H. Lu, Y. F. Yan and G. J. Fang, *Small*, 2017, **13**, 1601769.
209 W. Q. Wu, D. Chen, Y. B. Cheng and R. A. Caruso, *Sol. RRL*, 2017, **1**, 1700117.
210 H. H. Niu, C. L. Fang, X. T. Wei, H. Wang, L. Wan, Y. Li, X. L. Mao, J. Z. Xu and R. Zhou, *Dalton Trans.*, 2021, **50**, 6477–6487.
211 J. Chen, H. Dong, L. Zhang, J. Li, F. Jia, B. Jiao, J. Xu, X. Hou, J. Liu and Z. Wu, *J. Mater. Chem. A*, 2020, **8**, 2644–2653.
212 X. Gong, Q. Sun, S. Liu, P. Liao, Y. Shen, C. Grätzel, S. M. Zakeeruddin, M. Grätzel and M. Wang, *Nano Lett.*, 2018, **18**, 3969–3977.
213 J. Duan, Q. Xiong, B. Feng, Y. Xu, J. Zhang and H. Wang, *Appl. Surf. Sci.*, 2017, **391**, 677–683.
214 Y. Qiang, Y. Xie, Y. Qi, P. Wei, H. Shi, C. Geng and H. Liu, *Sol. Energy*, 2020, **201**, 523–529.
215 M. Hu, L. Zhang, S. She, J. Wu, X. Zhou, X. Li, D. Wang, J. Miao, G. Mi, H. Chen, Y. Tian, B. Xu and C. Cheng, *Sol. RRL*, 2020, **4**, 1900331.
216 H. Dong, S. Pang, Y. Xu, Z. Li, Z. Zhang, W. Zhu, D. Chen, H. Xi, Z. Lin, J. Zhang, Y. Hao and C. Zhang, *ACS Appl. Mater. Interfaces*, 2020, **12**, 54703–54710.
217 Y. W. Noh, I. S. Jin, K. S. Kim, S. H. Park and J. W. Jung, *J. Mater. Chem. A*, 2020, **8**, 17163–17173.
218 Z. Liu, K. Deng, J. Hu and L. Li, *Angew. Chem., Int. Ed.*, 2019, **58**, 11497–11504.

219 Y. Ai, W. Liu, C. Shou, J. Yan, N. Li, Z. Yang, W. Song, B. Yan, J. Sheng and J. Ye, *Sol. Energy*, 2019, **194**, 541–547.
220 Z. Zhang, J. Zhang, N. Chen and L. Qu, *Energy Environ. Sci.*, 2012, **5**, 8869–8890.
221 J. J. Yoo, G. Seo, M. R. Chua, T. G. Park, Y. Lu, F. Rotermund, Y. K. Kim, C. S. Moon, N. J. Jeon, J. P. Correa-Baena, V. Bulovic, S. S. Shin, M. G. Bawendi and J. Seo, *Nature*, 2021, **590**, 587–593.
222 B. Roose, C. M. Johansen, K. Dupraz, T. Jaouen, P. Aebi and U. Steiner, *J. Mater. Chem. A*, 2018, **6**, 1850–1857.
223 N. Ren, B. Chen, R. Li, P. Wang, S. Mazumdar, B. Shi, C. Zhu, Y. Zhao and X. Zhang, *Sol. RRL*, 2021, **5**, 2000795.
224 L. Xiong, M. Qin, C. Chen, J. Wen, G. Yang, Y. Guo, J. Ma, Q. Zhang, P. Qin, S. Li and G. Fang, *Adv. Funct. Mater.*, 2018, **28**, 1706276.
225 Q. Dong, C. Zhu, M. Chen, C. Jiang, J. Guo, Y. Feng, Z. Dai, S. K. Yadavalli, M. Hu, X. Cao, Y. Li, Y. Huang, Z. Liu, Y. Shi, L. Wang, N. P. Padture and Y. Zhou, *Nat. Commun.*, 2021, **12**, 973.
226 Q. Dong, M. Chen, Y. Liu, F. T. Eickemeyer, W. Zhao, Z. Dai, Y. Yin, C. Jiang, J. Feng, S. Jin, S. Liu, S. M. Zakeeruddin, M. Grätzel, N. P. Padture and Y. Shi, *Joule*, 2021, **5**, 1587–1601.
227 M. M. Tavakoli, F. Giordano, S. M. Zakeeruddin and M. Gratzel, *Nano Lett.*, 2018, **18**, 2428–2434.
228 (*a*) A. R. Verma, S. Pathak, A. K. Srivastava, S. Prawer and S. Tomljenovic-Hanic, *J. Alloys Compd.*, 2021, **876**, 160175; (*b*) B. S. Jiang, K. Lin and M. Cai, *Front. Chem.*, 2020, **8**, 580.
229 S. Faisal, H. Jan, S. A. Shah, S. Shah, A. Khan, M. T. Akbar, M. Rizwan, F. Jan, Wajidullah, N. Akhtar, A. Khattak and S. Syed, *ACS Omega*, 2021, **6**, 9709–9722.
230 R. T. Selvi, A. P. S. Prasanna, R. Niranjan, M. Kaushik, T. Devasena, J. Kumar, R. Chelliah, D.-H. Oh, S. Swaminathan and G. D. Venkatasubbu, *Appl. Surf. Sci.*, 2018, **449**, 603–609.
231 J. Prakash, K. S. Venkataprasanna and G. D. Venkatasubbu, *New J. Chem.*, 2022, **46**, 13325–13344.
232 J. Prakash, K. S. Venkataprasanna, D. Prema, S. M. Sahabudeen, S. D. Banita and G. D. Venkatasubbu, *Toxicol. Mech. Methods*, 2020, **30**, 508–525.
233 S. M. I. Rayyif, H. B. Mohammed, C. Curuțiu, A. C. Bîrcă, A. M. Grumezescu, B. Ș. Vasile, L. M. Dițu, V. Lazăr, M. C. Chifiriuc, G. Mihăescu and A. M. Holban, *Materials*, 2021, **14**, 3084.
234 Y. K. Mishra, R. Adelung, C. Röhl, D. Shukla, F. Spors and V. Tiwari, *Antiviral Res.*, 2011, **92**, 305–312.
235 A. Tavakoli, A. Ataei-Pirkooh, G. M. Sadeghi, F. Bokharaei-Salim, P. Sahrapour, S. J. Kiani, M. Moghoofei, M. Farahmand, D. Javanmard and S. H. Monavari, *Nanomedicine*, 2018, **13**, 2675–2690.
236 G. H. Attia, Y. S. Moemen, M. Youns, A. M. Ibrahim, R. Abdou and M. A. El Raey, *Colloids Surf., B*, 2021, **203**, 111724.
237 R. Medhi, P. Srinoi, N. Ngo, H.-V. Tran and T. R. Lee, *ACS Appl. Nano Mater.*, 2020, **3**, 8557–8580.
238 J. Zhang, H. Zeng, J. Gu, H. Li, L. Zheng and Q. Zou, Progress and Prospects on Vaccine Development against SARS-CoV-2, *Vaccines*, 2020, **8**, 153.
239 U. M. T. M. Gunathilaka, W. A. P. P. de Silva, S. P. Dunuweera and R. M. G. Rajapakse, *RSC Adv.*, 2021, **11**, 8857–8866.
240 P. P. Dhavan and B. L. Jadhav, *SN Appl. Sci.*, 2020, **2**, 843.
241 K. Velsankar, S. Sudhahar, G. M. aheshwaran and M. Krishna Kumar, *J. Photochem. Photobiol., B*, 2019, **200**, 111650.
242 A. B. Moghaddam, M. Moniri, S. Azizi, R. Abdul Rahim, A. Bin Ariff, M. Navaderi and R. Mohamad, *Genes*, 2017, **8**, 281.
243 M. M. Housseiny and E. Z. Gomaa, *J. Bot*, 2019, **59**, 319–337.
244 T. Zhang, E. Du, Y. Liu, J. Cheng, Z. Zhang, Y. Xu, S. Qi and Y. Chen, *Int. J. Nanomed.*, 2020, **15**, 1457–1468.
245 S. Matussin, M. H. Harunsani, A. L. Tan and M. M. Khan, *ACS Sustainable Chem. Eng.*, 2020, **8**, 3040–3054.
246 M. P. Nikolova and M. S. Chavali, *Biomimetics*, 2020, **5**, 27.
247 V. K. Vidhu and D. Philip, *Spectrochim. Acta, Part A*, 2015, **134**, 372–379.
248 A. Ayeshamariam, M. T. M. Begam, M. Jayachandran, G. P. Kumar and M. J. Bououdina, *Int. J. Bioassays*, 2013, **2**, 304–311.
249 A. Bhawna, K. Choudhary, A. Gupta, S. Kumar, P. Kumar, R. P. Singh, P. Singh and V. Kumar, *Front. Nanotechnol*, 2020, **2**, 595352.
250 M. Sathishkumar and S. Geethalakshmi, *Mater. Today: Proc.*, 2020, **20**, 54–63.
251 I. Fatimah, G. Purwiandono, H. Hidayat, S. Sagadevan, S. A. I. S. M. Ghazali, W.-C. Oh and R.-A. Doong, *Nanomaterials*, 2021, **11**, 3012.
252 S. A. Khan, S. Kanwal, K. Rizwan and S. Shahid, *Microb. Pathog.*, 2018, **125**, 366–384.
253 J. Trigilio, T. E. Antoine, I. Paulowicz, Y. K. Mishra, R. Adelung and D. Shukla, *PLoS One*, 2012, **7**, e48147.
254 G.-B. Hong and C.-J. Jiang, *Mater. Lett.*, 2017, **194**, 164–167.
255 R. V. Kamaraj P, A. Maruthapillai and D. Sundaramurthy, *World J. Pharm. Pharm. Sci.*, 2014, **3**, 382–388.
256 T. Sinha, M. Ahmaruzzaman, P. P. Adhikari and R. Bora, *ACS Sustainable Chem. Eng.*, 2017, **5**, 4645–4655.
257 H. Li, Q. Li, Y. Li, X. Sang, H. Yuan and B. Zheng, *Front. Bioeng. Biotechnol.*, 2020, **8**, 768.
258 H. Lv, C. Wu, X. Liu, A. Bai, Y. Cao, W. Shang, L. Hu and Y. Liu, *BioMed Res. Int.*, 2018, **2018**, 8526190.
259 A. P. S. Prasanna, K. S. Venkataprasanna, B. Pannerselvam, V. Asokan, R. S. Jeniffer and G. D. Venkatasubbu, *J. Fluoresc.*, 2020, **30**, 1075–1083.
260 W. Guo, C. Tan, K. Shi, J. Li, X.-X. Wang, B. Sun, X. Huang, Y.-Z. Long and P. Jiang, *Nanoscale*, 2018, **10**, 17751–17760.
261 Q. Xu, J. Wen and Y. Qin, *Nano Energy*, 2021, **86**, 106080.
262 X. Cao, Y. Xiong, J. Sun, X. Zhu, Q. Sun and Z. L. Wang, *Adv. Funct. Mater.*, 2021, 2102983.
263 J. Zhou, P. Fei, Y. Gu, W. Mai, Y. Gao, R. Yang, G. Bao and Z. L. Wang, *Nano Lett.*, 2008, **8**, 3973–3977.

264 J. Briscoe, E. Bilotti and S. Dunn, *Appl. Phys. Lett.*, 2012, **201**, 093902.
265 R. Zhang, H. Andersson, M. Olsen, M. Hummelgard, S. Edvardsson, H.-E. Nilsson and H. Olin, *Nano Energy*, 2014, **3**, 10–15.
266 R. Kurniawan, F. Willy, E. Nurfani, S. Muhammady, M. Sutjahja, T. Winata and Y. Darma, *Mater. Res. Exp.*, 2017, **4**, 024003.
267 A. Onodera and M. Takesada, *Advanced Ferroelectricity*, 2013, ch. 11, pp. 231–253.
268 P. Chand, A. Gaur and A. Kumar, *Adv. Mater. Lett.*, 2013, **4**, 220–2224.
269 Z. L. Wang, *Appl. Phys. A*, 2007, **88**, 7–15.
270 Y. Zhang and L. Li, *Nano Energy*, 2016, **22**, 533–538.
271 Z. L. Wang and J. Song, *Science*, 2006, **312**, 242.
272 M. K. Gupta, J.-H. Lee, K. Y. Lee and S.-W. Kim, *ACS Nano*, 2013, **7**, 8932–8939.
273 K. Y. Lee, J. Bae, S. M. Kim, J.-H. Lee, G. C. Yoon, M. K. Gupta, S. Kim, H. Kim, J. Park and S.-W. Kim, *Nano Energy*, 2014, **8**, 165–173.
274 K.-H. Kim, B. Kumar, K. Y. Lee, H.-K. Park, J.-H. Lee, H. H. Lee, H. Jun, D. Lee and S.-W. Kim, *Sci. Rep.*, 2013, **3**, 2017.
275 X. Q. Fang, J.-X. Liu and V. Gupta, *Nanoscale*, 2013, **5**, 1716–1726.
276 S. Dai, M. Gharbi, P. Sharma and H. S. Park, *J. Appl. Phys.*, 2011, **110**, 104305.
277 M. Minary-Jolandan, R. A. Bernal, I. Kuljanishvili, V. Parpoil and H. D. Espinosa, *Nano Lett.*, 2012, **12**, 970.
278 G. Lu, K. L. Huebner, L. E. Ocola, M. G. Josifovska and J. Chen, *J. Nanomaterials*, 2006, 60828.
279 D. A. Popescu and F. B. Verduraz, *Catal. Today*, 2001, **70**, 139–154.
280 Z. Huang, J. Zhu, Y. Hu, Y. Zhu, G. Zhu, L. Hu, Y. Zi and W. Huang, *Nanomaterials*, 2022, **12**, 632.
281 E. Elangovan and K. Ramamurthi, *J. Optoelectron. Adv. Mater.*, 2003, **5**, 45–54.
282 E. Kar, N. Bose, B. Dutta, S. Banerjee, N. Mukherjee and S. Mukherjee, *Energy Convers. Manage.*, 2019, **184**, 600–608.
283 D. Zhu, Y. Fu, W. Zang, Y. Zhao, L. Xing and X. Xue, *Sens. Actuators, B*, 2014, **205**, 12–19.
284 C. Pan, J. Zhai and Z. L. Wang, *Chem. Rev.*, 2019, **119**, 9303–9359.
285 C. Liu, M. Peng, A. Yu, J. Liu, M. Song, Y. Zhang and J. Zhai, *Nano Energy*, 2016, **26**, 417–424.
286 Y. Zhang, C. Liu, J. Liu, J. Xiong, J. Liu, K. Zhang, Y. Liu, M. Peng, A. Yu, A. Zhang, Y. Zhang, Z. Wang, J. Zhai and Z. L. Wang, *ACS Appl. Mater. Interfaces*, 2016, **8**, 1381–1387.
287 M. Song, Y. Liu, A. Yu, Y. Zhang, J. Zhai and Z. L. Wang, *Nano Energy*, 2019, **55**, 341–347.
288 F. Xue, L. Chen, J. Chen, J. Liu, L. Wang, M. Chen, Y. Pang, X. Yang, G. Gao, J. Zhai and Z. L. Wang, *Adv. Mater.*, 2016, **28**, 3391–3398.
289 Q. Zheng, M. Peng, Z. Liu, S. Li, R. Han, H. Ouyang, Y. Fan, C. Pan, W. Hu, J. Zhai, Z. Li and Z. L. Wang, *Sci. Adv.*, 2021, **7**, eabe7738.
290 J. Kaur and H. Singh, *J. Mater. Sci.: Mater. Electron.*, 2019, **30**, 4437–4445.
291 Y. H. Ko, G. Nagaraju and J. S. Yu, *Nanoscale Res. Lett.*, 2013, **8**, 511.
292 S. H. Shin, Y. H. Kim, M. H. Lee, J. Y. Jung, J. H. Seol and J. Nah, *ACS Nano*, 2014, **8**, 10844–10850.
293 S. N. Cha, J. S. Seo, S. M. Kim, H. J. Kim, Y. J. Park, S. W. Kim and J. M. Kim, *Adv. Mater.*, 2010, **22**, 4726–4730.
294 K. Verma, D. K. Bharti, S. Badatya, A. K. Srivastava and M. K. Gupta, *Nanoscale Adv.*, 2020, **2**, 2044–2051.
295 B. Yin, Y. Qiu, H. Zhang, J. Lei, Y. Chang, J. Ji, Y. Luo, Y. Zhao and L. Hu, *Nano Energy*, 2015, **14**, 95–101.
296 S. Lu, Q. Liao, J. Qi, S. Liu, Y. Liu, Q. Liang, G. Zhang and Y. Zhang, *Nano Res.*, 2016, **9**, 372–379.
297 R. Zhang, M. Hummelgård, M. Olsen, J. Örtegren and H. Olin, *Semicond. Sci. Technol.*, 2017, **32**, 054002.
298 Y. Hu, C. Xu, Y. Zhang, L. Lin, R. L. Snyde and Z. L. Wang, *Adv. Mater.*, 2011, **23**, 4068–4071.
299 Y. Xi, J. Song, S. Xu, R. Yang, Z. Gao, C. Hu and Z. L. Wang, *J. Mater. Chem.*, 2009, **19**, 9260–9264.
300 S. Stassi, C. Valentina, C. Ottone, A. Chiodoni, C. F. Pirri and G. Canavese, *Nano Energy*, 2015, **3**, 474–481.